Journal of Geophysical Research: Atmospheres

Correspondence to:
Z. Zhang,
Zhibo.Zhang@umbc.edu

A framework based on 2-D Taylor expansion for quantifying the impacts of subpixel reflectance variance and covariance on cloud optical thickness and effective radius retrievals based on the bispectral method

Z. Zhang[1,2], F. Werner[2], H.-M. Cho[2,3], G. Wind[4,5], S. Platnick[4], A. S. Ackerman[6], L. Di Girolamo[7], A. Marshak[4], and K. Meyer[4,8]

[1]Physics Department, UMBC, Baltimore, Maryland, USA, [2]Joint Center for Earth Systems Technology, UMBC, Baltimore, Maryland, USA, [3]Electronics and Telecommunications Research Institute, Daejeon, South Korea, [4]NASA Goddard Space Flight Center, Greenbelt, Maryland, USA, [5]Science Systems and Applications, Inc., Lanham, Maryland, USA, [6]NASA Goddard Institute for Space Studies, New York City, New York, USA, [7]Department of Atmospheric Sciences, University of Illinois at Urbana-Champaign, Urbana, Illinois, USA, [8]Universities Space Research Association, Columbia, Maryland, USA

Abstract The bispectral method retrieves cloud optical thickness (τ) and cloud droplet effective radius (r_e) simultaneously from a pair of cloud reflectance observations, one in a visible or near-infrared (VIS/NIR) band and the other in a shortwave infrared (SWIR) band. A cloudy pixel is usually assumed to be horizontally homogeneous in the retrieval. Ignoring subpixel variations of cloud reflectances can lead to a significant bias in the retrieved τ and r_e. In the literature, the retrievals of τ and r_e are often assumed to be independent and considered separately when investigating the impact of subpixel cloud reflectance variations on the bispectral method. As a result, the impact on τ is contributed only by the subpixel variation of VIS/NIR band reflectance and the impact on r_e only by the subpixel variation of SWIR band reflectance. In our new framework, we use the Taylor expansion of a two-variable function to understand and quantify the impacts of subpixel variances of VIS/NIR and SWIR cloud reflectances and their covariance on the τ and r_e retrievals. This framework takes into account the fact that the retrievals are determined by both VIS/NIR and SWIR band observations in a mutually dependent way. In comparison with previous studies, it provides a more comprehensive understanding of how subpixel cloud reflectance variations impact the τ and r_e retrievals based on the bispectral method. In particular, our framework provides a mathematical explanation of how the subpixel variation in VIS/NIR band influences the r_e retrieval and why it can sometimes outweigh the influence of variations in the SWIR band and dominate the error in r_e retrievals, leading to a potential contribution of positive bias to the r_e retrieval. We test our framework using synthetic cloud fields from a large-eddy simulation and real observations from Moderate Resolution Imaging Spectroradiometer. The predicted results based on our framework agree very well with the numerical simulations. Our framework can be used to estimate the retrieval uncertainty from subpixel reflectance variations in operational satellite cloud products and to help understand the differences in τ and r_e retrievals between two instruments.

1. Introduction

Among many satellite-based cloud remote sensing techniques, the bispectral solar reflective method ("bispectral method" hereafter) is a widely used method to infer cloud optical thickness (τ) and cloud droplet effective radius (r_e) from satellite observation of cloud reflectance [*Nakajima and King*, 1990]. This method uses cloud reflectance measurements from two spectral bands to simultaneously retrieve τ and r_e. One measurement is usually made in the visible or near-infrared (VIS/NIR) spectral region (e.g., 0.64 μm or 0.86 μm), where water absorption is negligible and therefore cloud reflection generally increases with τ. The other measurement is usually in the shortwave infrared (SWIR) spectral region (e.g., 2.1 μm or 3.7 μm), where water droplets are moderately absorptive and cloud reflectance generally decreases with increasing r_e for optically thick clouds. In practice, the bispectral method is often implemented utilizing a so-called look-up table (LUT). A couple of LUT examples are shown in Figure 1. Such LUTs contain precomputed bidirectional cloud reflectances at VIS/NIR and SWIR bands for various combinations of r_e and τ under different Sun-satellite viewing geometries and surface reflectances. Given the observed reflectances, the corresponding r_e and τ can be retrieved easily by searching and interpolating the proper LUT. The bispectral method has been adopted
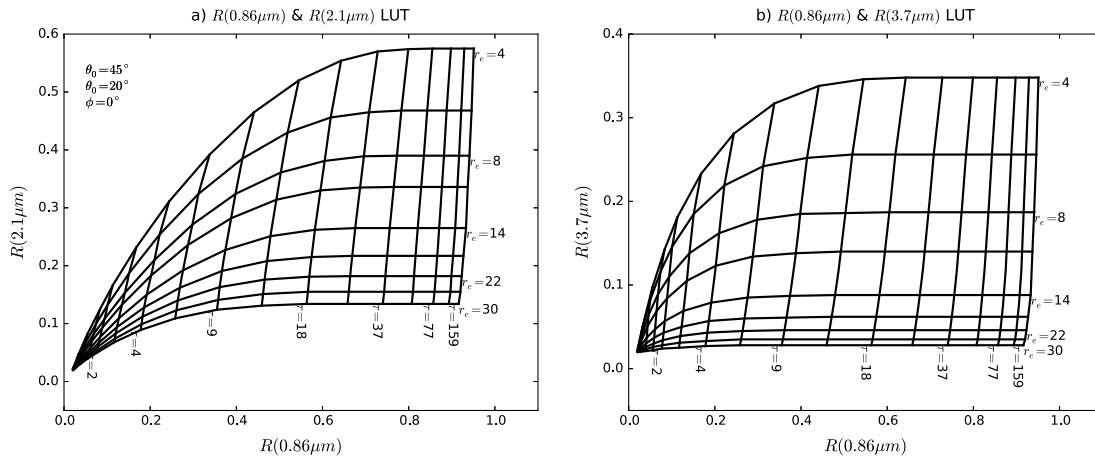
Figure 1. Examples of the look-up table of cloud bidirectional reflection functions as functions of cloud optical thickness and effective radius, based on the combination of (a) 0.86 μm and 2.1 μm bands and (b) 0.86 μm and 3.7 μm bands. Surface is assumed to be Lambertian with a reflectance of 0.02. Solar and viewing zenith angles are 45° and 20°, respectively. Relative azimuthal angle is 0°.

by a number of satellite missions, including Moderate Resolution Imaging Spectroradiometer (MODIS), Visible Infrared Imaging Radiometer Suite (VIIRS), and Spinning Enhanced Visible and Infrared Imager (SEVIRI) for operational retrievals of cloud properties (i.e., τ, r_e, and derived cloud liquid water path (LWP)) [*Platnick et al.*, 2003; *Roebeling et al.*, 2006; *Minnis et al.*, 2011; *Walther and Heidinger*, 2012]. Given the wide usage of the bispectral method, it is critical to study and understand its limitations and uncertainties.

The bispectral method makes several important assumptions about the cloud (or cloudy pixels). First, within a cloudy pixel, the cloud is assumed to be horizontally homogenous (referred to as the "homogenous pixel assumption"). Second, it is assumed that the pixels are independent from each other, in the sense that there is no net interpixel transport of radiation (often referred to as the "independent pixel assumption"). Under these assumptions, clouds are considered to be "plane-parallel." In addition to plane-parallel cloud assumptions, clouds are often assumed to be vertically homogenous in the operational algorithms. Furthermore, the size spectrum of cloud particles is often assumed to follow certain analytical distributions, such as the single modal gamma or lognormal size distributions [e.g., *Nakajima and King*, 1990; *Dong et al.*, 1997]. These assumptions may be reasonable for certain types of clouds, such as closed-cell, nonprecipitating stratocumulus, but become problematic for others, such as broken trade wind cumuli or precipitating clouds [*Di Girolamo et al.*, 2010; *Painemal and Zuidema*, 2011; *Zhang and Platnick*, 2011; *Liang and Girolamo*, 2013; *Zhang*, 2013]. As elucidated in numerous previous studies, when real clouds deviate from these assumptions, the r_e and τ retrievals from the bispectral method can suffer from large errors and uncertainties [e.g., *Várnai and Marshak*, 2002; *Kato et al.*, 2006; *Marshak et al.*, 2006; *Zhang and Platnick*, 2011; *Zhang et al.*, 2012; *Zhang*, 2013; *Liang et al.*, 2015].

The focus of this study is the homogenous pixel assumption. Our objective is to develop a unified framework for understanding and quantifying the impacts of subpixel level unresolved reflectance variations on r_e and τ retrievals based on the bispectral method. A number of previous studies have already made substantial progress in this direction. It has been known for a long time that at the spatial scale of climate model grids (e.g., ~10^2 km) approximating inhomogeneous cloud fields with plane-parallel clouds can lead to significant biases in shortwave solar radiation [e.g., *Harshvardhan and Randall*, 1985; *Cahalan et al.*, 1994; *Barker*, 1996]. *Cahalan et al.* [1994] described an elegant theoretical framework based on a fractal cloud model to explain the influence of small-scale horizontal variability of τ on the averaged cloud reflectance in the visible spectral region (R_{VIS}). It is shown that the averaged reflectance $\overline{R_{VIS}(\tau_i)}$, where τ_i denotes the subpixel-scale cloud optical thickness, is smaller than the reflectance that corresponds to the averaged cloud optical thickness $\overline{\tau_i}$, i.e., $\overline{R_{VIS}(\tau_i)} < R_{VIS}(\overline{\tau_i})$. This inequality relation is well known as the "plane-parallel homogenous bias" (referred to as PPHB), which is a result of the nonlinear dependence of R_{VIS} on τ, i.e., $\frac{\partial^2 R_{VIS}}{\partial \tau^2} < 0$. The implication of the PPHB for τ retrievals from R_{VIS} is illustrated using an example shown in Figure 2a. Here we assume that one half of an inhomogeneous pixel is covered by a thinner cloud with $\tau_1 = 5$ and the other half by a thicker
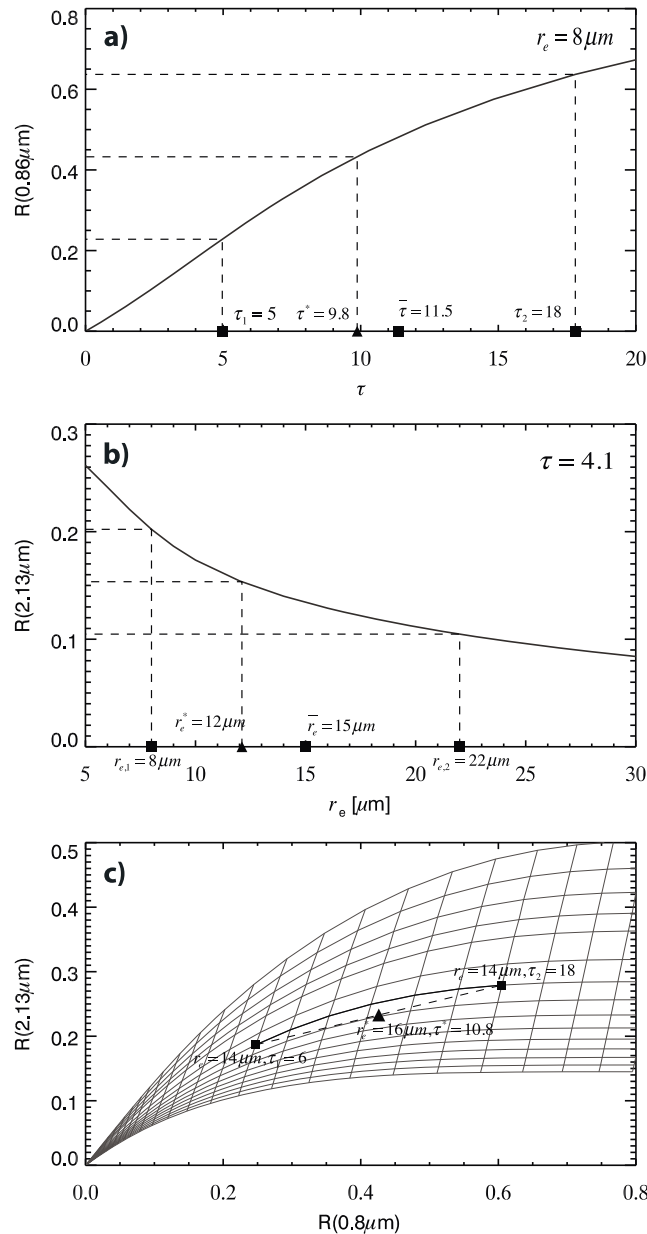
Figure 2. (a) Example to illustrate the PPHB bias proposed in *Cahalan et al.* [1994] for the retrieval of τ retrieval, (b) example to illustrate the PPHB bias proposed in *Marshak et al.* [2006], and (c) example to illustrate the r_e retrieval bias caused by subpixel τ variability proposed in *Zhang and Platnick* [2011] and *Zhang et al.* [2012]. See text for details. Solar and viewing zenith angles are assumed to be 20° and 0°, and relative azimuth angle is assumed to be 30°.

cloud with $\tau_2 = 18$ (both clouds with $r_e = 8$ μm). Because of the PPHB, the retrieved cloud optical thickness $\tau^* = 9.8$ based on the averaged reflectance $\overline{R} = [R(\tau_1) + R(\tau_2)]/2$ is significantly smaller than the linear average of the subpixel τ, i.e., $\overline{\tau} = 11.5$. The impacts of PPHB on satellite-based cloud property retrievals and the implications have been investigated in a number of studies [*Oreopoulos and Davies*, 1998; *Pincus et al.*, 1999; *Oreopoulos et al.*, 2007].

We note that the variation of cloud reflectance may be a result of varying cloud properties but may also be caused by 3-D radiative effects. For example, a cloudy pixel can be perfectly homogenous in terms of cloud properties, but the surrounding pixels can cast a shadow on part of this pixel leading to subpixel reflectance variations [*Marshak et al.*, 2006]. A variety of such 3-D effects that cannot be explained by the 1-D plane-parallel radiative transfer theory have been identified, and their impacts on cloud property retrievals have been investigated in previous studies [*Davis and Marshak*, 2010]. In reality, the PPHB is inevitably entangled with the 3-D radiative transfer effects and other uncertainties such as the impact of instrument noise in the retrieval. It is difficult, if not impossible, to separate them. Following the literature, we shall refer to the impact of subpixel cloud reflectance variation on cloud property retrievals as the PPHB while keeping in mind that the subpixel cloud reflectance variation can also result from 3-D radiative effects and may not reflect the true variation of subpixel cloud properties.

Recently, as the interests in aerosol-cloud interactions have grown, there is an increasing attention on the impacts of small-scale cloud variations on the satellite-based r_e retrievals [e.g., *Kato et al.*, 2006; *Marshak et al.*, 2006; *Zhang and Platnick*, 2011; *Zhang et al.*, 2012; *Liang et al.*, 2015]. *Marshak et al.* [2006] pointed out that similar to the PPHB, the nonlinear dependence of the SWIR band cloud reflectance (R_{SWIR}) on r_e can also lead to significant biases on r_e retrievals, which is demonstrated in Figure 2b. Here one half of an inhomogeneous pixel is covered by a cloud with $r_e = 8$ μm and the other half by a cloud with $r_e = 22$ μm. Both parts have the same $\tau = 4.1$. As shown in the figure, the retrieved $r_e^* = 12$ μm based on the averaged reflectance is significantly smaller than the linear average of subpixel $\overline{r_e} = 15$ μm, similar to the PPHB of τ in Figure 2a. It must be noted that in the framework of *Marshak et al.* [2006] the retrievals of r_e and τ are considered separately and assumed to be independent from one another. However, as *Marshak et al.* [2006] pointed out,

this assumption is valid only for "large enough" τ and r_e (typically, $r_e > 5\,\mu m$ and $\tau > 10$). As one can see from the shape of the LUT in Figure 1, R_{SWIR} is not completely orthogonal to R_{VIS}, especially when τ is small. As a result, the retrievals of r_e and τ are not independent from one another. *Marshak et al.* [2006] suspected that some cases with large r_e bias in their simulations might be the result of this mutual dependence of r_e and τ retrievals. *Zhang and Platnick* [2011] showed that the subpixel variance of τ can have a significant impact on the r_e retrieval, which is illustrated in the example in Figure 2c. In this hypothetical case, an inhomogeneous pixel is assumed to be covered by a thinner cloud with $\tau_1 = 6$ in one half and a thicker cloud with $\tau_2 = 18$ in the other. Both clouds have the same $r_e = 14\,\mu m$. Note that in this case the subpixel reflectance variation is solely caused by the variability in τ. If the r_e retrieval were independent from the τ retrieval, then the retrieved r_e would be 14 μm. The solid triangle in the figure indicates the location of R_{VIS} and R_{SWIR} averaged over the pixel, i.e., the "observation." The retrieved $\tau^* = 10.8$ is smaller than the averaged $\bar{\tau} = 12$ as a result of the PPHB. However, the retrieved $r_e^* = 16$ is 2 μm larger than the expected value of 14 μm. This positive bias in the r_e retrieval, apparently caused by the subpixel variability of τ, cannot be explained by the framework of *Marshak et al.* [2006] in which the r_e retrieval is assumed to be independent from the τ retrieval. *Zhang and Platnick* [2011] and *Zhang et al.* [2012] also found that the magnitude of the positive r_e retrieval bias caused by the subpixel variability of τ is dependent on the SWIR band chosen for the r_e retrieval. These studies showed that the same subpixel τ variability tends to induce a larger bias in retrieved r_e using the less absorptive 2.1 μm band (referred to as $r_{e,2.1}$) than that using the more absorptive 3.7 μm band (referred to as $r_{e,3.7}$). This spectral dependence provides an important explanation for the fact that the MODIS operational $r_{e,2.1}$ retrievals for water clouds are often significantly larger than the $r_{e,3.7}$ retrievals, especially when clouds have large subpixel heterogeneity [*Zhang and Platnick*, 2011; *Cho et al.*, 2015].

The aforementioned studies have undoubtedly shed important light on the impact of subpixel cloud variability on r_e and τ retrievals based on the bispectral method. However, several questions still remain. For example, an important question is how to reconcile the negative r_e bias discussed in *Marshak et al.* [2006] and the positive r_e bias discussed in *Zhang and Platnick* [2011] and *Zhang et al.* [2012]. Indeed, this is the main question we will address in this study. In the light of previous studies, here we develop a new mathematical framework to provide a more comprehensive and complete understanding of the impact of subpixel cloud variability on r_e and τ retrievals based on the bispectral method. The paper is organized as follows: We formulate the problem in section 2. We introduce our mathematical framework in section 3, test and validate it using two examples in section 4, and discuss its applications in section 5.

2. Statement of the Problem

In the bispectral method, r_e and τ are retrieved from a pair of cloud reflectance observations, one in VIS/NIR and the other in SWIR. From this point of view, we can define r_e and τ as

$$
\begin{aligned}
\tau &\equiv \tau(R_{VIS}, R_{SWIR}) \\
r_e &\equiv r_e(R_{VIS}, R_{SWIR}),
\end{aligned}
\tag{1}
$$

where R_{VIS} and R_{SWIR} are the observed reflectances in the VIS/NIR (denoted by subscript "VIS" for short) and SWIR bands, respectively. Assume that an instrument with a relatively coarse spatial resolution observes a horizontally inhomogeneous cloudy pixel in its field of view. The observed cloud reflectances are $\overline{R_{VIS}}$ and $\overline{R_{SWIR}}$, where the overbar denotes the spatial average. Now if we use another instrument with a finer spatial resolution to observe the same area covered by the coarser resolution pixel, we can obtain high-resolution observations, $R_{VIS,i}$ and $R_{SWIR,i}$, $i = 1, 2, \ldots N$, where the number N depends on the relative sizes of the pixels. The high-resolution measurements provide the information on the variance and covariance of R_{VIS} and R_{SWIR} at the subpixel scale. Each subpixel observation $R_{VIS,i}$ and $R_{SWIR,i}$ can be specified as the deviation from the mean value $\overline{R_{VIS}}$ and $\overline{R_{SWIR}}$ as

$$
\begin{aligned}
R_{VIS,i} &= \overline{R_{VIS}} + \Delta R_{VIS,i} \\
R_{SWIR,i} &= \overline{R_{SWIR}} + \Delta R_{SWIR,i}
\end{aligned}
\quad ; i = 1, 2 \ldots N.
\tag{2}
$$

It naturally follows that the spatial average $\overline{\Delta R_{VIS,i}} = \overline{\Delta R_{SWIR,i}} = 0$. Based on the coarse-resolution reflectance observations $\overline{R_{VIS}}$ and $\overline{R_{SWIR}}$, we can retrieve $\tau(\overline{R_{VIS}}, \overline{R_{SWIR}})$ and $r_e(\overline{R_{VIS}}, \overline{R_{SWIR}})$. From the high-resolution,

subpixel observations $R_{\text{VIS},i}$ and $R_{\text{SWIR},i}$, we can retrieve $\tau(R_{\text{VIS},i}, R_{\text{SWIR},i})$ and $r_e(R_{\text{VIS},i}, R_{\text{SWIR},i})$. The differences $\Delta\tau$ and Δr_e, defined as

$$\Delta\tau = \tau\left(\overline{R_{\text{VIS}}}, \overline{R_{\text{SWIR}}}\right) - \overline{\tau\left(R_{\text{VIS},i}, R_{\text{SWIR},i}\right)}$$
$$\Delta r_e = r_e\left(\overline{R_{\text{VIS}}}, \overline{R_{\text{SWIR}}}\right) - \overline{r_e\left(R_{\text{VIS},i}, R_{\text{SWIR},i}\right)},$$
(3)

are considered in this, as well as previous studies, as the biases caused by the homogeneous pixel assumption in r_e and τ retrievals [*Cahalan and Joseph*, 1989; *Marshak et al.*, 2006; *Zhang et al.*, 2012].

Consideration of equation (3) raises a few important questions. What are the sign and magnitude of $\Delta\tau$ and Δr_e? How do they depend on the subpixel $R_{\text{VIS},i}$ and $R_{\text{SWIR},i}$? Addressing these questions could help improve the understanding of the biases caused by ignoring the subpixel reflectance variation in bispectral r_e and τ retrievals. Furthermore, since performing high-resolution retrievals can be computationally expensive, another important question is whether it is possible to estimate $\overline{\tau\left(R_{\text{VIS},i}, R_{\text{SWIR},i}\right)}$ and $\overline{r_e\left(R_{\text{VIS},i}, R_{\text{SWIR},i}\right)}$ from the coarse-resolution retrievals and the statistics of subpixel reflectance observations, even without doing time-consuming high-resolution retrievals. If this proved possible, then it is a very efficient way to estimate the biases and uncertainties caused by the homogenous pixel assumption. These questions are the focus of this study and will be addressed in the next section.

Before proceeding, we need to clarify two points. First, the $\Delta\tau$ and Δr_e in equation (3) are the differences between two sets of retrievals, *not* the differences between the retrievals and "true" cloud properties. As mentioned earlier, subpixel reflectance variations can be due to subpixel-scale cloud property variations but may also be caused by 3-D radiative effects. If the former is dominant, then $\Delta\tau$ and Δr_e provide an estimate of the PPHB and can be used to correct the coarse-resolution retrievals to better represent the true cloud properties. However, if 3-D effects are the dominant cause of the subpixel reflectance variation, then $\Delta\tau$ and Δr_e can be considered a quantitative index of the 3-D effects on the retrievals. Second, our scope is to study the connections between retrieval biases $\Delta\tau$ and Δr_e with subpixel observations $R_{\text{VIS},i}$ and $R_{\text{SWIR},i}$. We simply take $R_{\text{VIS},i}$ and $R_{\text{SWIR},i}$ as given inputs. Here we do not seek to explain the characteristics of $R_{\text{VIS},i}$ and $R_{\text{SWIR},i}$ (e.g., their mean values, variances, and covariance) or their dependence on cloud properties. Neither do we try to explain how 3-D radiative effects and instrument characteristics influence $R_{\text{VIS},i}$ and $R_{\text{SWIR},i}$.

3. A Unified Mathematical Framework

In this section, we will introduce a comprehensive framework that is able to reconcile and unify the theoretical understandings provided by *Marshak et al.* [2006], *Zhang and Platnick* [2011], and *Zhang et al.* [2012]. To investigate the sign and magnitude of $\Delta\tau$ and Δr_e, we first expand $\tau(R_{\text{VIS},i}, R_{\text{SWIR},i})$ and $r_e(R_{\text{VIS},i}, R_{\text{SWIR},i})$ into two-dimensional Taylor series of $R_{\text{VIS},i}$ and $R_{\text{SWIR},i}$. Take $r_e(R_{\text{VIS},i}, R_{\text{SWIR},i})$ for example. The expansion is

$$r_e\left(R_{\text{VIS},i}, R_{\text{SWIR},i}\right) = r_e\left(\overline{R_{\text{VIS}}} + \Delta R_{\text{VIS},i}, \overline{R_{\text{SWIR}}} + \Delta R_{\text{SWIR},i}\right)$$
$$= r_e\left(\overline{R_{\text{VIS}}}, \overline{R_{\text{SWIR}}}\right) + \underbrace{\frac{\partial r_e\left(\overline{R_{\text{VIS}}}, \overline{R_{\text{SWIR}}}\right)}{\partial R_{\text{VIS}}}\Delta R_{\text{VIS},i} + \frac{\partial r_e\left(\overline{R_{\text{VIS}}}, \overline{R_{\text{SWIR}}}\right)}{\partial R_{\text{SWIR}}}\Delta R_{\text{SWIR},i}}_{\text{Linear terms}} +$$
$$\underbrace{\frac{1}{2}\frac{\partial^2 r_e\left(\overline{R_{\text{VIS}}}, \overline{R_{\text{SWIR}}}\right)}{\partial R_{\text{VIS}}^2}\Delta R_{\text{VIS},i}^2 + \frac{\partial^2 r_e\left(\overline{R_{\text{VIS}}}, \overline{R_{\text{SWIR}}}\right)}{\partial R_{\text{VIS}}\partial R_{\text{SWIR}}}\Delta R_{\text{VIS},i}\Delta R_{\text{SWIR},i} + \frac{1}{2}\frac{\partial^2 r_e\left(\overline{R_{\text{VIS}}}, \overline{R_{\text{SWIR}}}\right)}{\partial R_{\text{SWIR}}^2}\Delta R_{\text{SWIR},i}^2}_{\text{Second-order terms}} + \varepsilon.$$
(4)

where ε is the truncation error if higher-order derivative terms are neglected. If we take the spatial average of equation (4) and neglect ε, all the linear terms (i.e., $\frac{\partial r_e\left(\overline{R_{\text{VIS}}}, \overline{R_{\text{SWIR}}}\right)}{\partial R_{\text{VIS}}}\Delta R_{\text{VIS},i}$ and $\frac{\partial r_e\left(\overline{R_{\text{VIS}}}, \overline{R_{\text{SWIR}}}\right)}{\partial R_{\text{SWIR}}}\Delta R_{\text{SWIR},i}$) vanish because $\overline{\Delta R_{\text{VIS},i}} = \overline{\Delta R_{\text{SWIR},i}} = 0$. Thus, only second-order terms in equation (4) remain after the spatial average:

$$\overline{r_e\left(R_{\text{VIS},i}, R_{\text{SWIR},i}\right)} \approx r_e\left(\overline{R_{\text{VIS}}}, \overline{R_{\text{SWIR}}}\right) + \frac{1}{2}\frac{\partial^2 r_e\left(\overline{R_{\text{VIS}}}, \overline{R_{\text{SWIR}}}\right)}{\partial R_{\text{VIS}}^2}\sigma_{\text{VIS}}^2 + \frac{\partial^2 r_e\left(\overline{R_{\text{VIS}}}, \overline{R_{\text{SWIR}}}\right)}{\partial R_{\text{VIS}}\partial R_{\text{SWIR}}}\text{cov}(R_{\text{VIS}}, R_{\text{SWIR}})$$
$$+ \frac{1}{2}\frac{\partial^2 r_e\left(\overline{R_{\text{VIS}}}, \overline{R_{\text{SWIR}}}\right)}{\partial R_{\text{SWIR}}^2}\sigma_{\text{SWIR}}^2,$$
(5)
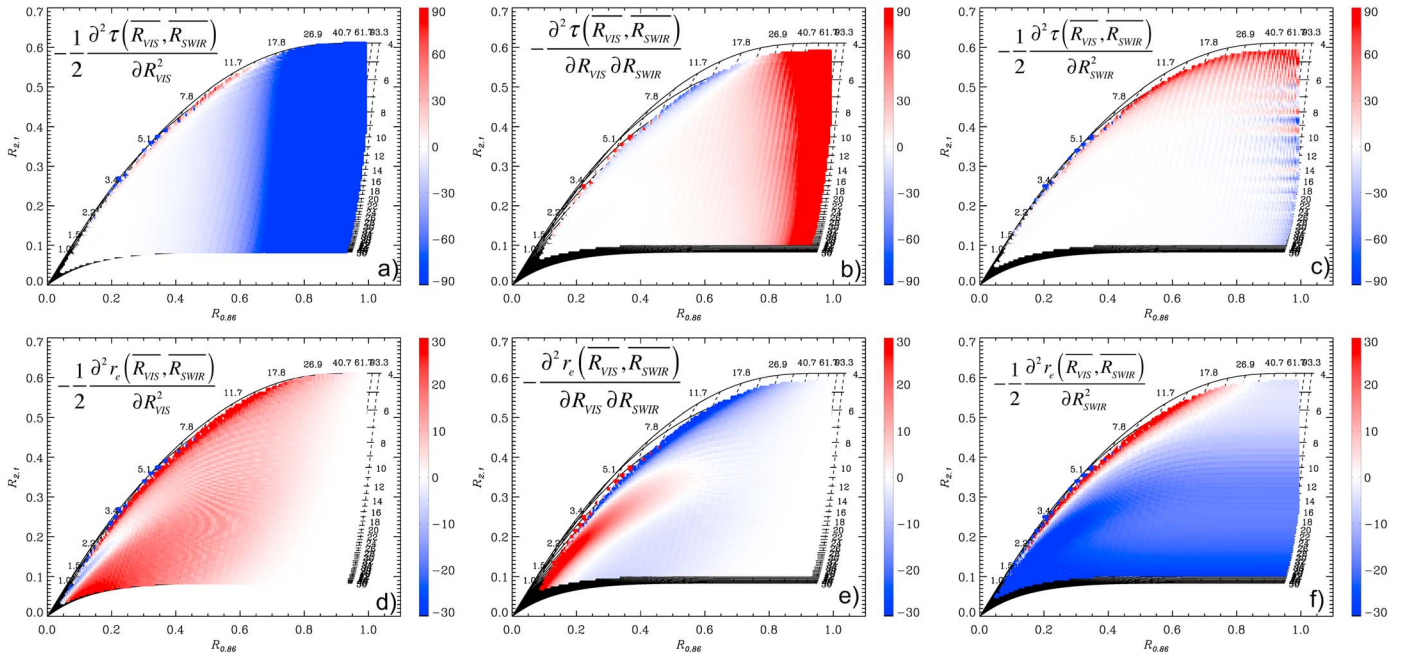
Figure 3. The sign and magnitude of each second derivative term in equation (8) derived from the $R_{0.86}$ and $R_{2.1}$ LUT. (a) $-\frac{1}{2}\frac{\partial^2 \tau\left(\overline{R_{VIS}},\overline{R_{SWIR}}\right)}{\partial R_{VIS}^2}$, (b) $-\frac{\partial^2 \tau\left(\overline{R_{VIS}},\overline{R_{SWIR}}\right)}{\partial R_{VIS}\partial R_{SWIR}}$, (c) $-\frac{1}{2}\frac{\partial^2 \tau\left(\overline{R_{VIS}},\overline{R_{SWIR}}\right)}{\partial R_{SWIR}^2}$, (d) $-\frac{1}{2}\frac{\partial^2 r_e\left(\overline{R_{VIS}},\overline{R_{SWIR}}\right)}{\partial R_{VIS}^2}$, (e) $-\frac{\partial^2 r_e\left(\overline{R_{VIS}},\overline{R_{SWIR}}\right)}{\partial R_{VIS}\partial R_{SWIR}}$, and (f) $-\frac{1}{2}\frac{\partial^2 r_e\left(\overline{R_{VIS}},\overline{R_{SWIR}}\right)}{\partial R_{SWIR}^2}$. Solar and viewing zenith angles are assumed to be 20° and 0°, relative azimuth angle is assumed to be 30°.

where $\sigma_{VIS}^2 = \overline{\Delta R_{VIS,i}^2}$ and $\sigma_{SWIR}^2 = \overline{\Delta R_{SWIR,i}^2}$ are the spatial variances of $R_{VIS,i}$ and $R_{SWIR,i}$, respectively, and cov (R_{VIS}, R_{SWIR}) is the spatial covariance of $R_{VIS,i}$ and $R_{SWIR,i}$. Substituting equation (5) into equation (3), we obtain the following formula for Δr_e:

$$\Delta r_e = r_e\left(\overline{R_{VIS}},\overline{R_{SWIR}}\right) - \overline{r_e\left(R_{VIS,i},R_{SWIR,i}\right)}$$
$$= -\frac{1}{2}\frac{\partial^2 r_e\left(\overline{R_{VIS}},\overline{R_{SWIR}}\right)}{\partial R_{VIS}^2}\sigma_{VIS}^2 - \frac{\partial^2 r_e\left(\overline{R_{VIS}},\overline{R_{SWIR}}\right)}{\partial R_{VIS}\partial R_{SWIR}}\mathrm{cov}(R_{VIS},R_{SWIR}) - \frac{1}{2}\frac{\partial^2 r_e\left(\overline{R_{VIS}},\overline{R_{SWIR}}\right)}{\partial R_{SWIR}^2}\sigma_{SWIR}^2. \quad (6)$$

Following the same procedure, we can derive the formula for $\Delta\tau$ as

$$\Delta\tau = \tau\left(\overline{R_{VIS}},\overline{R_{SWIR}}\right) - \overline{\tau\left(R_{VIS,i},R_{SWIR,i}\right)}$$
$$= -\frac{1}{2}\frac{\partial^2 \tau\left(\overline{R_{VIS}},\overline{R_{SWIR}}\right)}{\partial R_{VIS}^2}\sigma_{VIS}^2 - \frac{\partial^2 \tau\left(\overline{R_{VIS}},\overline{R_{SWIR}}\right)}{\partial R_{VIS}\partial R_{SWIR}}\mathrm{cov}(R_{VIS},R_{SWIR}) - \frac{1}{2}\frac{\partial^2 \tau\left(\overline{R_{VIS}},\overline{R_{SWIR}}\right)}{\partial R_{SWIR}^2}\sigma_{SWIR}^2. \quad (7)$$

Equations (6) and (7) can be combined into a matrix form as follows:

$$\begin{pmatrix} \Delta\tau \\ \Delta r_e \end{pmatrix} = \begin{pmatrix} -\frac{1}{2}\frac{\partial^2 \tau\left(\overline{R_{VIS}},\overline{R_{SWIR}}\right)}{\partial R_{VIS}^2} & -\frac{\partial^2 \tau\left(\overline{R_{VIS}},\overline{R_{SWIR}}\right)}{\partial R_{VIS}\partial R_{SWIR}} & -\frac{1}{2}\frac{\partial^2 \tau\left(\overline{R_{VIS}},\overline{R_{SWIR}}\right)}{\partial R_{SWIR}^2} \\ -\frac{1}{2}\frac{\partial^2 r_e\left(\overline{R_{VIS}},\overline{R_{SWIR}}\right)}{\partial R_{VIS}^2} & -\frac{\partial^2 r_e\left(\overline{R_{VIS}},\overline{R_{SWIR}}\right)}{\partial R_{VIS}\partial R_{SWIR}} & -\frac{1}{2}\frac{\partial^2 r_e\left(\overline{R_{VIS}},\overline{R_{SWIR}}\right)}{\partial R_{SWIR}^2} \end{pmatrix} \begin{pmatrix} \sigma_{VIS}^2 \\ \mathrm{cov} \\ \sigma_{SWIR}^2 \end{pmatrix}. \quad (8)$$

Equation (8) is the central equation of our framework for quantifying the impact of subpixel reflectance variance on r_e and τ retrievals. Equation (8) decomposes the impact of subpixel cloud reflectance variability on the τ and r_e retrievals based on the bispectral method into two parts: (1) the magnitude of the subpixel reflectance variance and covariance specified by the vector $(\sigma_{VIS}^2, \mathrm{cov}, \sigma_{SWIR}^2)^T$ (referred to as "subpixel variance vector") and (2) the matrix of the second-order derivatives of the LUT with respect to R_{VIS} and R_{SWIR} (referred to as "matrix of second derivatives"). Given the LUT, the matrix of second derivatives can be easily derived from straightforward numerical differentiation. An example of such a derived matrix based on the LUT for the 0.86 μm reflectance ($R_{0.86}$) and 2.1 μm reflectance ($R_{2.1}$) is shown in Figure 3. The values of the second
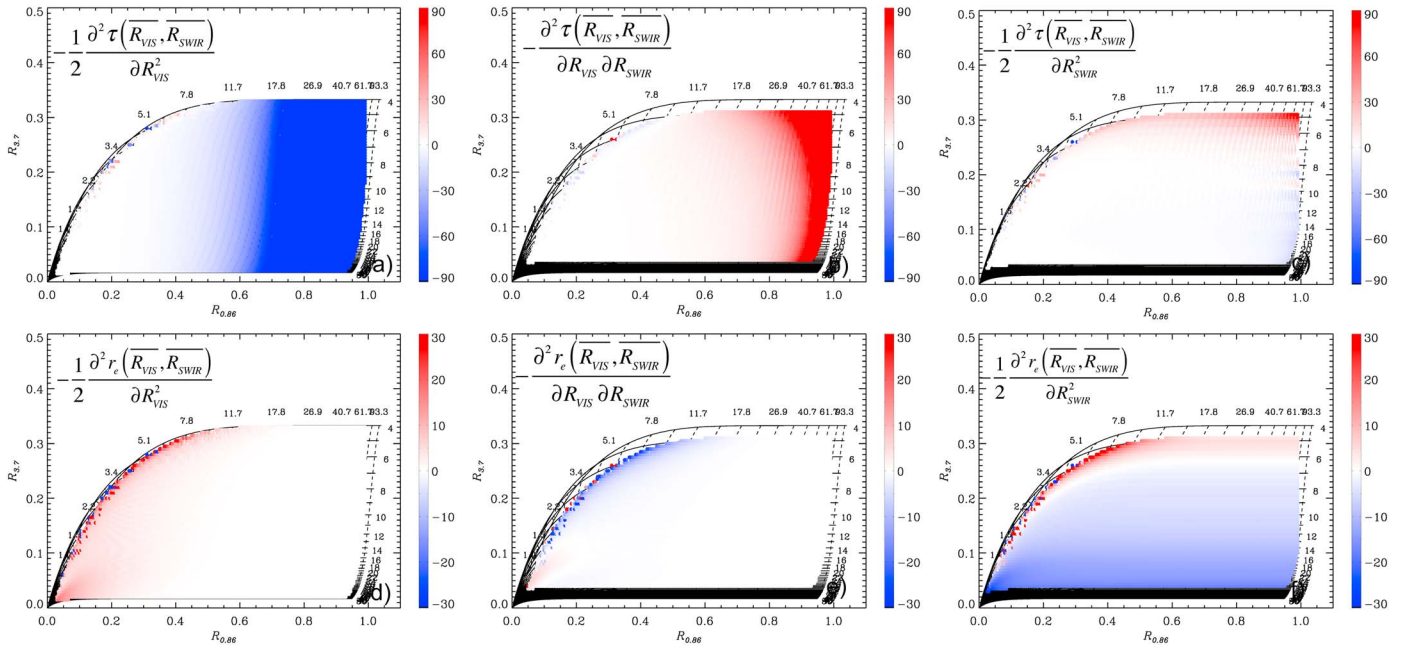
Figure 4. Same as Figure 3 except for the $R_{0.86}$ and $R_{3.7}$ LUT. Solar and viewing zenith angles are assumed to be 20° and 0°, and relative azimuth angle is assumed to be 30°.

derivatives for the grids of LUT are indicated by the color bar. Note that the sign of $\Delta\tau$ or Δr_e is determined both by the second derivatives and the subpixel variance vector $(\sigma^2_{\text{VIS}}, \text{cov}, \sigma^2_{\text{SWIR}})^T$. While σ^2_{VIS} and σ^2_{SWIR} are positive definite, the covariance term can be negative.

It is clear from equation (8) that the τ and r_e retrievals are influenced not only by the subpixel variation of the primary band (i.e., R_{VIS} for τ and R_{SWIR} for r_e) but also by the variation of the secondary band (i.e., R_{SWIR} for τ and R_{VIS} for r_e), as well as the covariance of the two bands R_{VIS} and R_{SWIR}. Therefore, it reconciles and unifies the theoretical frameworks in *Marshak et al.* [2006], *Zhang and Platnick* [2011], and *Zhang et al.* [2012]. In particular, the impact of the PPHB on τ and r_e, described in *Marshak et al.* [2006], corresponds to the upper left term, $-\frac{1}{2}\frac{\partial^2 \tau(\overline{R_{\text{VIS}}},\overline{R_{\text{SWIR}}})}{\partial R^2_{\text{VIS}}}$ (Figure 3a), and lower right term, $-\frac{1}{2}\frac{\partial^2 r_e(\overline{R_{\text{VIS}}},\overline{R_{\text{SWIR}}})}{\partial R^2_{\text{SWIR}}}$ (Figure 3f) in the second derivatives matrix, respectively. As shown in Figure 3, both terms are generally negative over the most part of the LUT. This is consistent with the findings of *Marshak et al.* [2006] where ignoring subpixel variability tends to result in an underestimation of the pixel average of the retrieved quantity if τ and r_e retrievals are considered separately and independently (i.e., negative $\Delta\tau$ and Δr_e). On the other hand, $\Delta\tau$ and Δr_e are also influenced by other terms in the matrix. Physically, these terms arise from the fact that both R_{VIS} and R_{SWIR} are dependent not only on τ but also on r_e. For example, the $-\frac{1}{2}\frac{\partial^2 r_e(\overline{R_{\text{VIS}}},\overline{R_{\text{SWIR}}})}{\partial R^2_{\text{VIS}}}$ term in Figure 3d is mostly positive in the region of the LUT with τ between about 1.5 and 20 and r_e between about 10 and 28 μm. This term competes with the negative $-\frac{1}{2}\frac{\partial^2 r_e(\overline{R_{\text{VIS}}},\overline{R_{\text{SWIR}}})}{\partial R^2_{\text{SWIR}}}$ term in determining the sign and size of Δr_e. In some cases, when σ^2_{VIS} is large as in the example in Figure 2c, the influence of $-\frac{1}{2}\frac{\partial^2 r_e(\overline{R_{\text{VIS}}},\overline{R_{\text{SWIR}}})}{\partial R^2_{\text{VIS}}}$ may be stronger, leading to a positive Δr_e, as argued in *Zhang and Platnick* [2011] and *Zhang et al.* [2012].

Some new terms that have not been explained in previous studies, e.g., the cross terms $-\frac{\partial^2 \tau(\overline{R_{\text{VIS}}},\overline{R_{\text{SWIR}}})}{\partial R_{\text{VIS}}\partial R_{\text{SWIR}}}$ in Figure 3b and $-\frac{\partial^2 r_e(\overline{R_{\text{VIS}}},\overline{R_{\text{SWIR}}})}{\partial R_{\text{VIS}}\partial R_{\text{SWIR}}}$ in Figure 3e, have also emerged from equation (8). These two terms generally have the opposite sign to those of the $-\frac{1}{2}\frac{\partial^2 \tau(\overline{R_{\text{VIS}}},\overline{R_{\text{SWIR}}})}{\partial R^2_{\text{VIS}}}$ and $-\frac{1}{2}\frac{\partial^2 r_e(\overline{R_{\text{VIS}}},\overline{R_{\text{SWIR}}})}{\partial R^2_{\text{SWIR}}}$ term, respectively. Because the covariance cov is generally positive, the cross terms seem to counteract the effects of $-\frac{1}{2}\frac{\partial^2 \tau(\overline{R_{\text{VIS}}},\overline{R_{\text{SWIR}}})}{\partial R^2_{\text{VIS}}}$ and $-\frac{1}{2}\frac{\partial^2 r_e(\overline{R_{\text{VIS}}},\overline{R_{\text{SWIR}}})}{\partial R^2_{\text{SWIR}}}$ on $\Delta\tau$ and Δr_e.

Equation (8) also provides a quantitative explanation for why subpixel inhomogeneity has different impacts on the r_e retrievals based on different SWIR bands (i.e., $r_{e,2.1}$ versus $r_{e,3.7}$). Figure 4 shows an example of the

matrix of second derivatives for the $R_{0.86}$ and $R_{3.7}$ combination. In comparison with the $R_{0.86}$ and $R_{2.1}$ combination in Figure 3, the $-\frac{1}{2}\frac{\partial^2 r_e\left(\overline{R_{VIS}},\overline{R_{SWIR}}\right)}{\partial R_{VIS}^2}$ term in Figure 4d is significantly smaller. This suggests that the same subpixel inhomogeneity in the 0.86 μm band (i.e., same σ_{VIS}^2) has a stronger impact on $r_{e,2.1}$ than it does on $r_{e,3.7}$. Because this term tends to lead to a positive Δr_e bias, it could be an important reason that the MODIS $r_{e,2.1}$ retrievals are often found to be significantly larger than the $r_{e,3.7}$ results, in particular for inhomogeneous pixels [*Painemal and Zuidema*, 2011; *Zhang and Platnick*, 2011; *Zhang et al.*, 2012; *Cho et al.*, 2015].

As analyzed above, in comparison with previous studies the framework described in equation (8) provides us with a more comprehensive explanation of the bias in τ and r_e retrievals caused by the homogenous pixel assumption. This framework may be useful in a variety of applications. It can be used to quantify $\Delta\tau$ and Δr_e if the subpixel variances and covariance $\left(\sigma_{VIS}^2, \ \mathrm{cov}, \ \sigma_{SWIR}^2\right)^T$ are known, as shown in the example in the next section. The $\Delta\tau$ and Δr_e can then in turn be used to estimate the uncertainties and potential biases in τ and r_e retrievals due to ignoring the subpixel reflectance variability in the bispectral method. Our framework can also be used to understand the differences among retrievals based on instruments with different spatial resolutions.

Finally, it is worth mentioning that equation (8) can be rewritten in a slightly different form as follows:

$$\begin{pmatrix}\Delta\tau \\ \Delta r_e\end{pmatrix} = \begin{pmatrix} -\frac{1}{2}\frac{\partial^2\tau\left(\overline{R_{VIS}},\overline{R_{SWIR}}\right)}{\partial R_{VIS}^2}\left(\overline{R_{VIS}}\right)^2 & -\frac{\partial^2\tau\left(\overline{R_{VIS}},\overline{R_{SWIR}}\right)}{\partial R_{VIS}\partial R_{SWIR}}\left(\overline{R_{VIS}}\cdot\overline{R_{SWIR}}\right) & -\frac{1}{2}\frac{\partial^2\tau\left(\overline{R_{VIS}},\overline{R_{SWIR}}\right)}{\partial R_{SWIR}^2}\left(\overline{R_{SWIR}}\right)^2 \\ -\frac{1}{2}\frac{\partial^2 r_e\left(\overline{R_{VIS}},\overline{R_{SWIR}}\right)}{\partial R_{VIS}^2}\left(\overline{R_{VIS}}\right)^2 & -\frac{\partial^2 r_e\left(\overline{R_{VIS}},\overline{R_{SWIR}}\right)}{\partial R_{VIS}\partial R_{SWIR}}\left(\overline{R_{VIS}}\cdot\overline{R_{SWIR}}\right) & -\frac{1}{2}\frac{\partial^2 r_e\left(\overline{R_{VIS}},\overline{R_{SWIR}}\right)}{\partial R_{SWIR}^2}\left(\overline{R_{SWIR}}\right)^2 \end{pmatrix}\begin{pmatrix}H_{\sigma_{VIS}}^2 \\ H_{cov}^2 \\ H_{\sigma_{SWIR}}^2\end{pmatrix}$$

$$(9)$$

where $H_{\sigma_{VIS}}^2 = \sigma_{VIS}^2/\left(\overline{R_{VIS}}\right)^2, H_{\sigma_{SWIR}}^2 = \sigma_{SWIR}^2/\left(\overline{R_{SWIR}}\right)^2$, and $H_{COV} = \mathrm{cov}(R_{VIS},R_{SWIR})/\left(\overline{R_{VIS}}\cdot\overline{R_{SWIR}}\right)$. Note that $H_{\sigma_{VIS}}$ has been used in previous studies as an index of subpixel inhomogeneity, in particular for MODIS cloud property retrievals [e.g., *Liang et al.*, 2009; *Di Girolamo et al.*, 2010; *Zhang and Platnick*, 2011; *Zhang et al.*, 2012; *Cho et al.*, 2015]. Therefore, although equations (9) and (8) are equivalent, some readers may find $\left(H_{\sigma_{VIS}}^2, H_{cov}, H_{\sigma_{SWIR}}^2\right)^T$ more familiar than $\left(\sigma_{VIS}^2, \ \mathrm{cov}, \ \sigma_{SWIR}^2\right)^T$.

It is important to point out that equations (8) and (9) hold true, whether the subpixel reflectance variations (i.e., nonzero $\left(\sigma_{VIS}^2, \ \mathrm{cov}, \ \sigma_{SWIR}^2\right)^T$) are attributable to subpixel-scale cloud property variations, 3-D radiative effects, or both. It is the interpretation of the resultant $\Delta\tau$ and Δr_e that is dependent on the circumstances and needs to be made with caution.

Finally, it is critical to note that we made an important assumption in the derivation of $\Delta\tau$ or Δr_e; that is, the truncation error ε in the Taylor expansion is negligible. This term is a summation of all the higher-order derivatives. Take r_e, for example, where the kth-order derivative has the form

$$\frac{1}{k!}\frac{d^k r_e}{dR^k} = \sum_{0\leq m\leq k}\frac{1}{m!(k-m)!}\frac{\partial^k r_e}{\partial R_{vis}^m\partial R_{vis}^{k-m}}\left(\overline{R_{VIS}},\overline{R_{SWIR}}\right)\Delta R_{VIS}^m\Delta R_{SWIR}^{k-m}.$$

$$(10)$$

Because there is no analytical solution to the higher-order derivatives, we can only assess the validity of this assumption and evaluate the accuracy of our framework numerically, which is done in the next section.

4. Numerical Tests

In this section, we evaluate the accuracy and limits of our mathematical framework using two examples. The main objective is to assess, through case studies, if the higher-order derivative terms are negligible so that our framework in equation (8) provides an accurate estimate of the PPHB.

4.1. Cloud Fields From Large-Eddy Simulation

In the first example, we test our framework using a synthetic cloud field simulated from a large-eddy simulations (LES) model (DHARMA) with bin microphysics [*Ackerman et al.*, 2004]. The LES case is based on an idealized case study [*Stevens et al.*, 2010] from the Atlantic Trade Wind Experiment (ATEX), with a diagnostic treatment of aerosol, specified to have a uniform number concentration of 40 cm^{-3}. The ATEX simulation represents a trade wind cumulus case under a sharp inversion. The ATEX simulation has a domain size of ($9.6\times9.6\times3$) km, with a uniform horizontal grid of $\Delta x = \Delta y = 100$ m and a fixed vertical grid spacing of $\Delta z = 40$ m. Further details of the
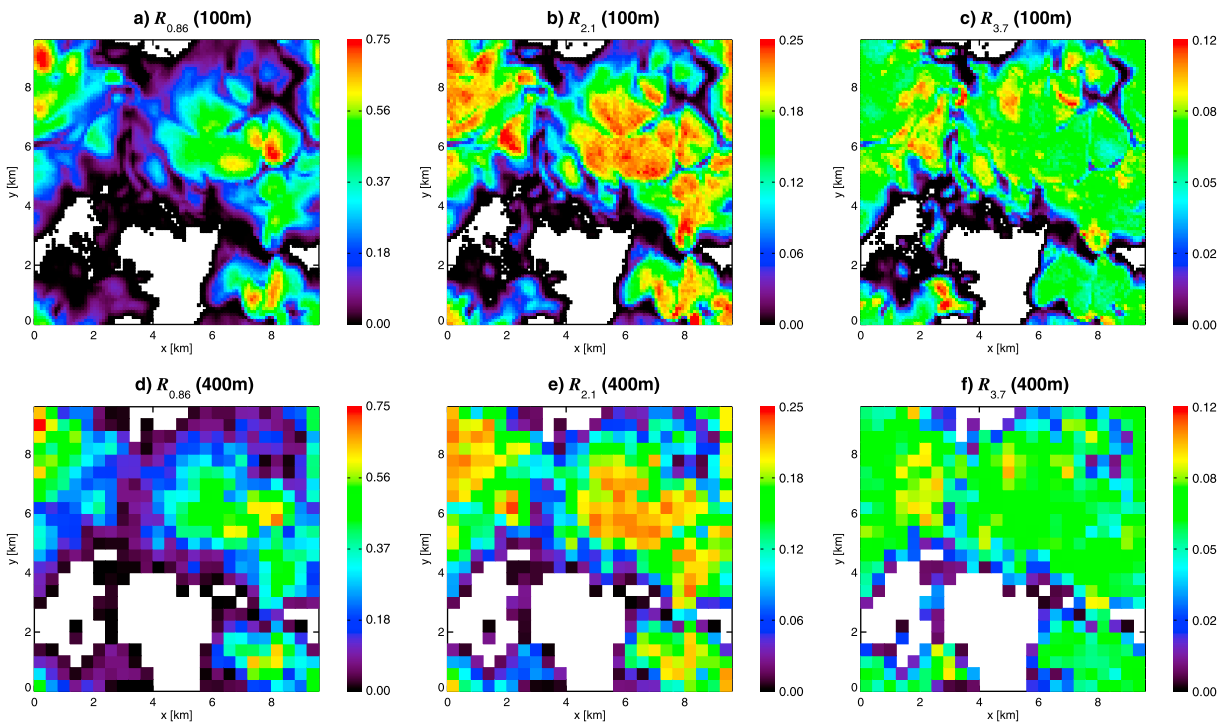
Figure 5. Simulated (a) 0.86 μm, (b) 2.1 μm, and (c) 3.7 μm bidirectional reflectances at 100 m resolution for the LES cloud field. (d–f) 400 m bidirectional reflectances averaged from 100 m resolution simulations.

model setup for the LES case are provided in *Zhang et al.* [2012]. The droplet size distributions from the LES are used to drive the radiative transfer simulations. The solar zenith and azimuth angle are set to 20° and 30°, respectively. For simplicity, the surface is assumed to be black. Both 1-D and 3-D radiative transfer simulations were performed, using the discrete ordinates radiative transfer [*Stamnes et al.*, 1988] and the I3RC models
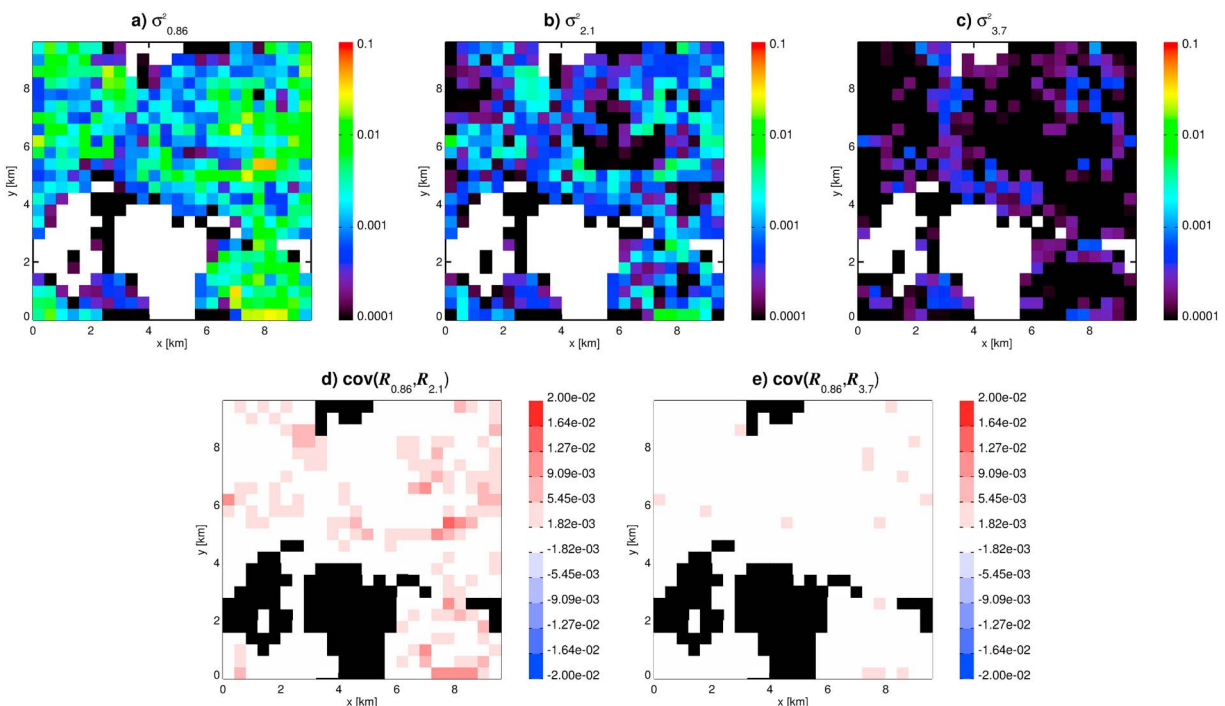
Figure 6. The subpixel reflectance variance (a) $\sigma^2_{0.86}$, (b) $\sigma^2_{2.1}$, and (c) $\sigma^2_{3.7}$ and covariances (d) $\text{cov}(R_{0.86}, R_{2.1})$ and (e) $\text{cov}(R_{0.86}, R_{3.7})$ for the LES case in Figure 5.
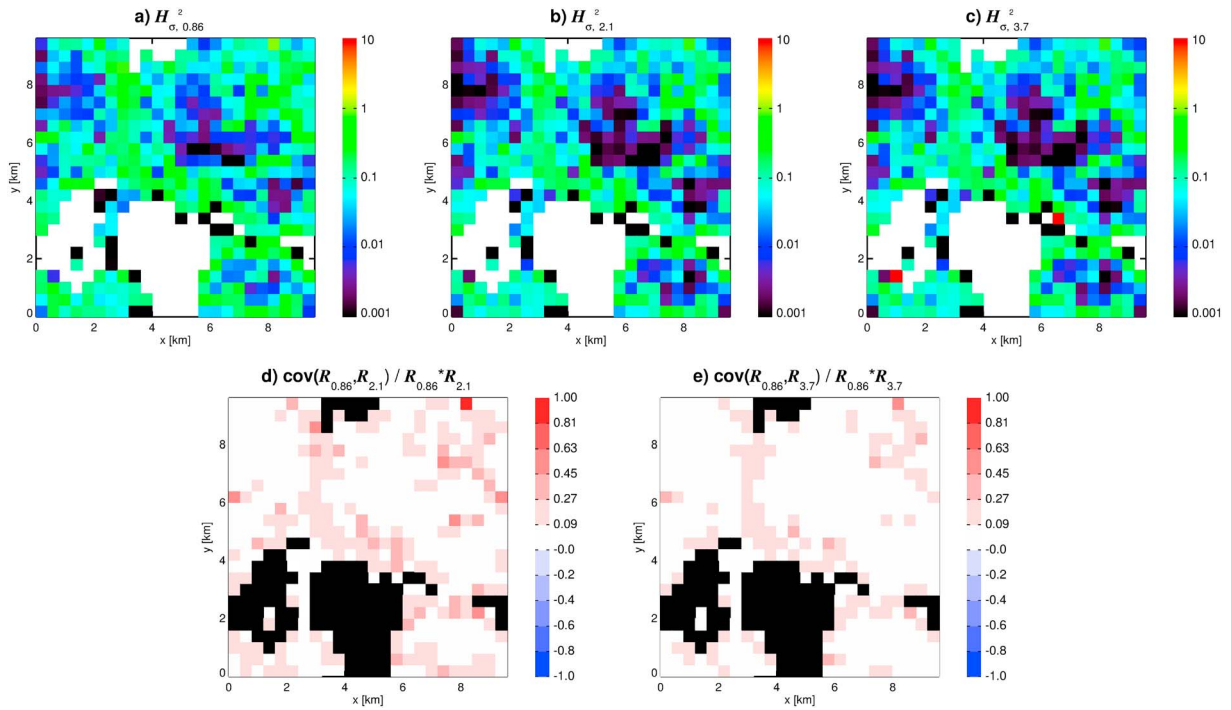
Figure 7. The subpixels (a) $H^2_{\sigma_{0.86}}$, (b) $H^2_{\sigma_{2.1}}$, and (c) $H^2_{\sigma_{3.7}}$ and relative covariances (d) $\mathrm{cov}(R_{0.86}, R_{2.1})/(\overline{R_{0.86}} \cdot \overline{R_{2.1}})$ and (e) $\mathrm{cov}(R_{0.86}, R_{3.7})/(\overline{R_{0.86}} \cdot \overline{R_{3.7}})$ for the LES case in Figure 5.

[*Pincus and Evans*, 2009], respectively. We focus on the 3-D results because they are more representative of real retrievals. The 1-D results are similar and are therefore not shown here.

We first run radiative transfer simulations at the 100 m horizontal resolution of the LES grid. Figures 5a–5c show the simulated 100 m cloud bidirectional reflectances at nadir-viewing angle for the 0.86 μm, 2.1 μm,
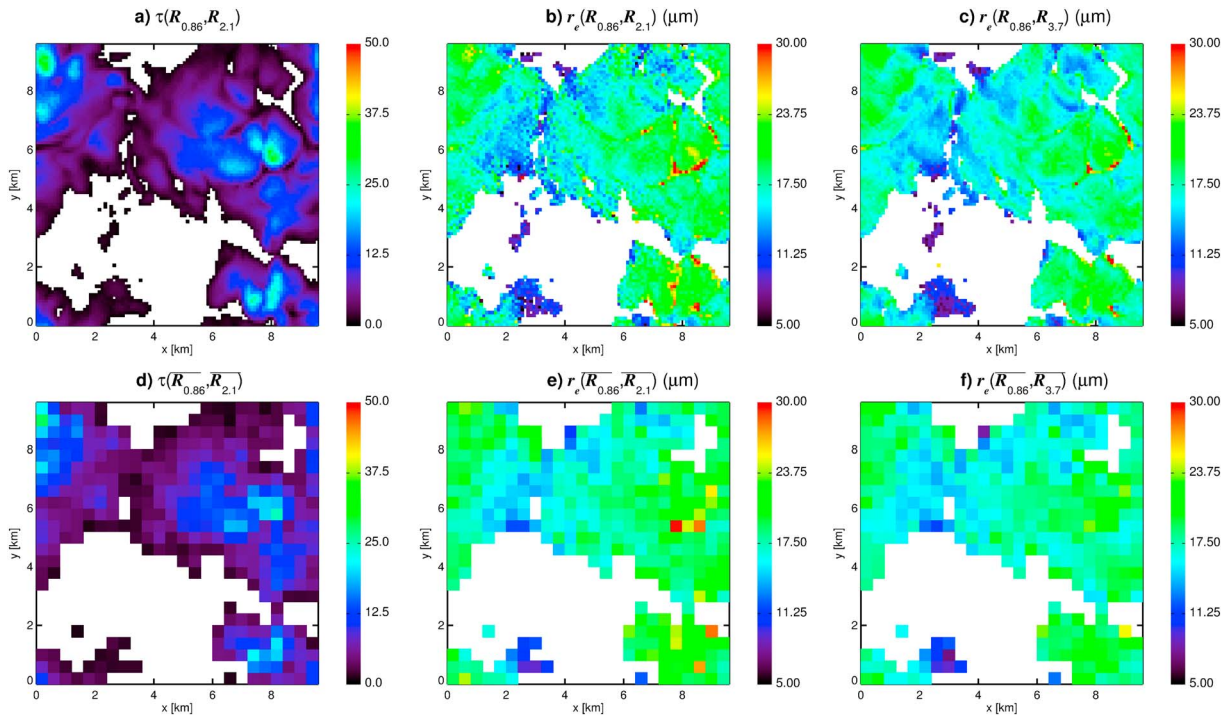
Figure 8. Retrievals of (a) τ, (b) $r_{e,2.1}$, and (c) $r_{e,3.7}$ based on the 100 m reflectances for the LES case in Figure 5. (d–f) Similar retrievals based on 400 m reflectances.
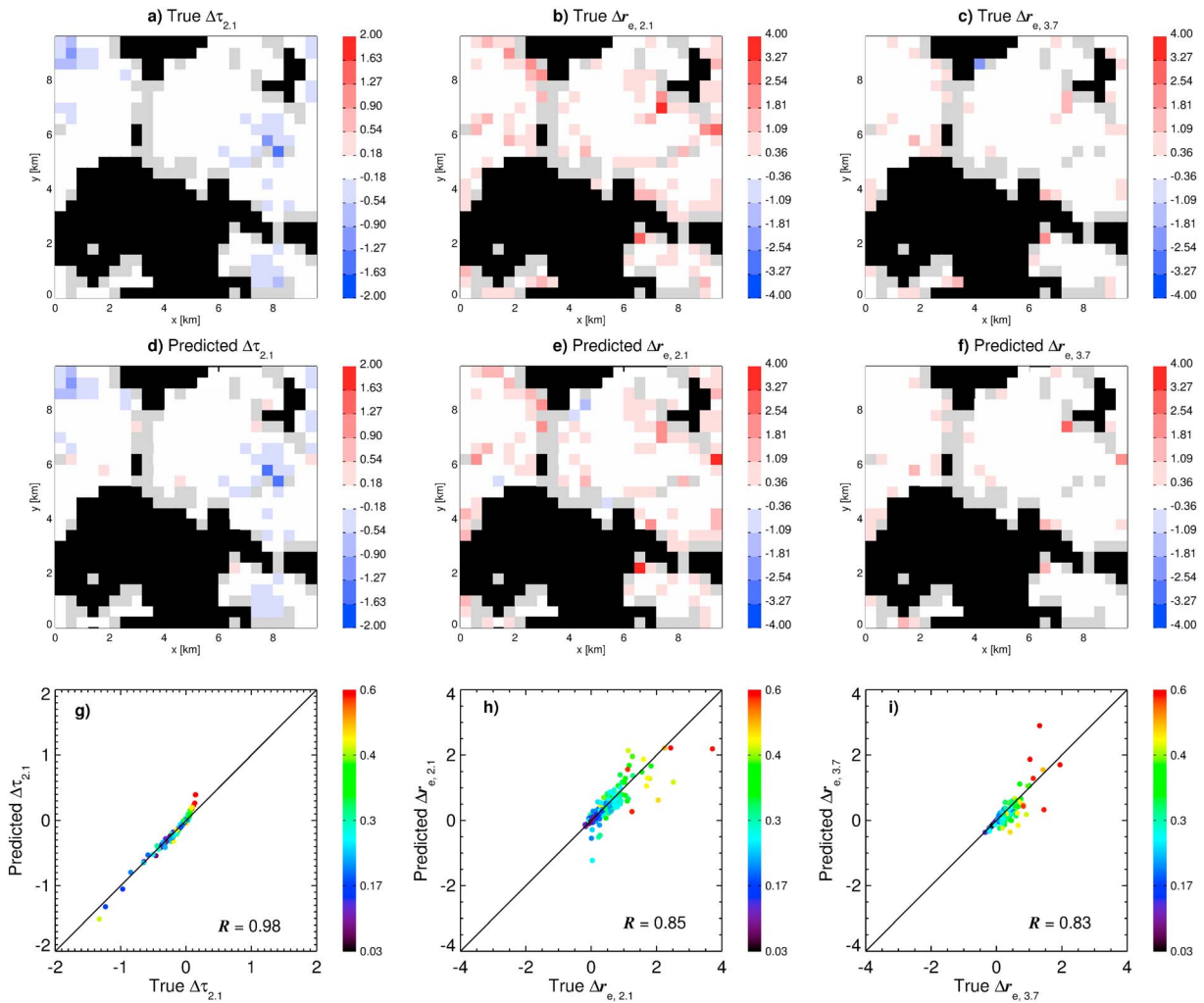
Figure 9. Derived (a) $\Delta\tau$, (b) $\Delta r_{e,2.1}$, and (c) $\Delta r_{e,3.7}$ based on equation (3). (d–f) The corresponding results obtained based on equation (8). (g–i) The pixel-to-pixel comparisons, in which the colors indicate the value of the subpixel inhomogeneity index $H_{\sigma_{0.86}}$.

and 3.7 μm MODIS bands, respectively. Subsequently, the 100 m reflectances are aggregated to 400 m to simulate the coarse-resolution observations, which are shown in Figures 5d–5f. Obviously, for each 400 m pixel we have 4×4 100 m pixels that can be used to derive the variances and covariances of the subpixel reflectances. Figure 6 shows the subpixel reflectance variances ($\sigma_{0.86}^2$, $\sigma_{2.1}^2$, and $\sigma_{3.7}^2$) and covariances (cov($R_{0.86}, R_{2.1}$) and cov($R_{0.86}, R_{3.7}$)) derived from 100 m reflectances. Because of the large, order-of-magnitude differences between $R_{0.86}$, $R_{2.1}$, and $R_{3.7}$, $\sigma_{0.86}^2$ is substantially larger than $\sigma_{2.1}^2$, which in turn is substantially larger than $\sigma_{3.7}^2$. Both covariances cov($R_{0.86}, R_{2.1}$) and cov($R_{0.86}, R_{3.7}$) are generally positive, indicating a general positive correlation between SWIR and VIS/NIR band cloud reflectances. This is not surprising because $R_{2.1}$ and $R_{3.7}$ do increase with τ when the cloud is optically thin. Only for optically thick clouds do $R_{2.1}$ and $R_{3.7}$ become independent from $R_{0.86}$. Figure 7 shows the reflectance variances and covariances normalized by the mean reflectances squared, i.e., $H_{\sigma_{0.86}}^2$, $H_{\sigma_{2.1}}^2$, and $H_{\sigma_{3.7}}^2$ and cov($R_{0.86}, R_{2.1}$)$/\left(\overline{R_{0.86}} \cdot \overline{R_{2.1}}\right)$ and cov($R_{0.86}, R_{3.7}$) $/\left(\overline{R_{0.86}} \cdot \overline{R_{3.7}}\right)$. After the normalization, $H_{\sigma_{0.86}}^2$, $H_{\sigma_{2.1}}^2$, and $H_{\sigma_{3.7}}^2$ are more comparable in terms of magnitude. In addition, cloud edges are seen to have larger subpixel inhomogeneity than the center of the cloud, which has also been found in MODIS observations [*Zhang and Platnick*, 2011; *Liang and Girolamo*, 2013].

The τ retrievals based on the simulated 100 m cloud reflectances ($R_{0.86}$ and $R_{2.1}$ combination) are shown in Figure 8a, which closely follow the $R_{0.86}$ observations in Figure 5a. The τ retrievals based on the $R_{0.86}$ and $R_{3.7}$ combination are mostly identical and therefore not shown. The $r_{e,2.1}$ and $r_{e,3.7}$ retrievals based on the
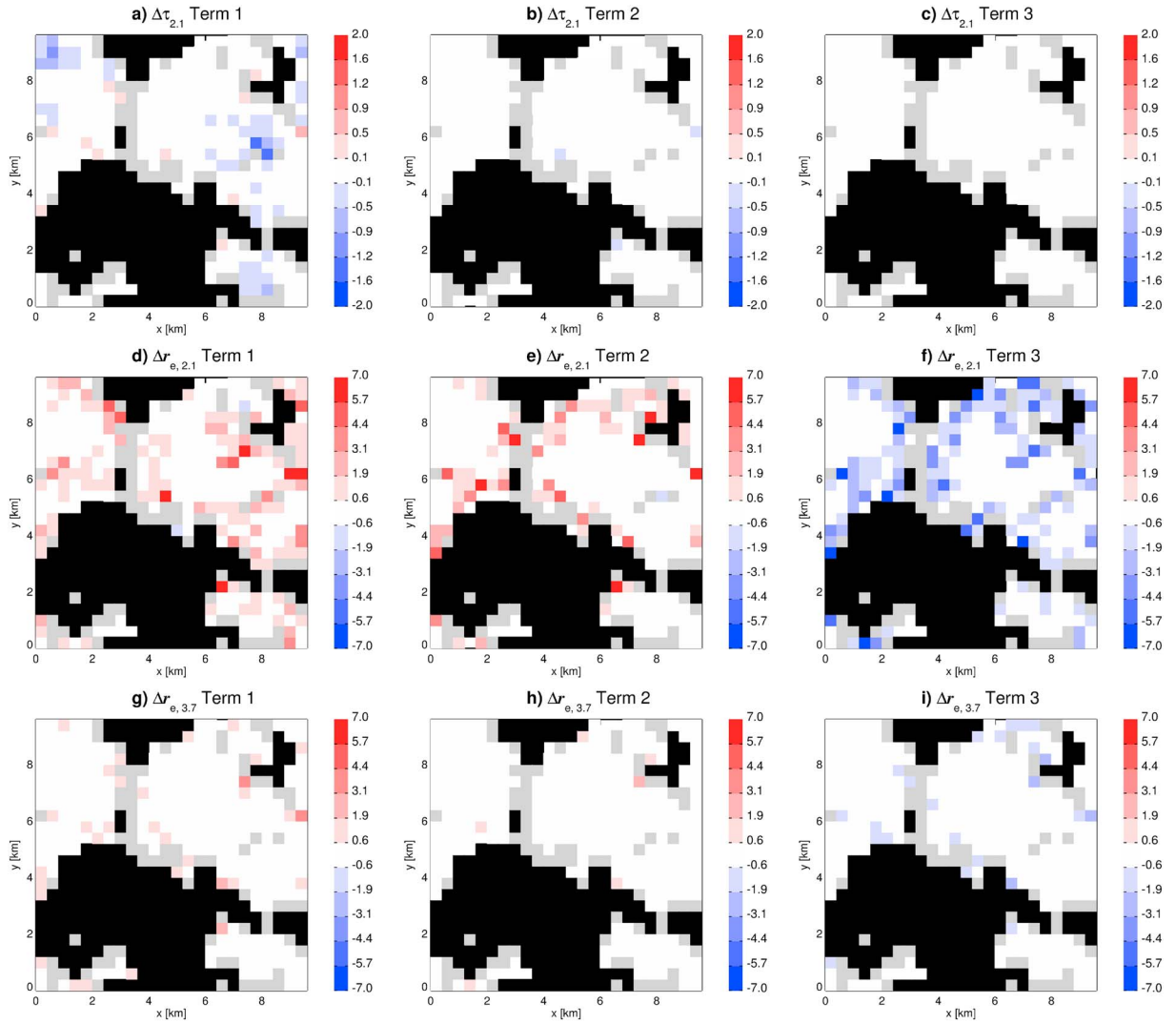
Figure 10. The decomposition of $\Delta\tau$ and Δr_e into the contributions from each term in the matrix of second derivative. (a) Contribution of $-\frac{1}{2}\frac{\partial^2 \tau\left(\overline{R_{0.86}},\overline{R_{2.1}}\right)}{\partial R_{0.86}^2}\cdot\sigma_{0.86}^2$ to $\Delta\tau$, (b) contribution of $-\frac{1}{2}\frac{\partial^2 \tau\left(\overline{R_{0.86}},\overline{R_{2.1}}\right)}{\partial R_{0.86}\partial R_{2.1}}\cdot \text{cov}(R_{0.86},R_{2.1})$ to $\Delta\tau$, (c) contribution of $-\frac{1}{2}\frac{\partial^2 \tau\left(\overline{R_{0.86}},\overline{R_{2.1}}\right)}{\partial R_{2.1}^2}\cdot\sigma_{2.1}^2$ to $\Delta\tau$, (d) contribution of $-\frac{1}{2}\frac{\partial^2 r_e\left(\overline{R_{0.86}},\overline{R_{2.1}}\right)}{\partial R_{0.86}^2}\cdot\sigma_{0.86}^2$ to $\Delta r_{e,2.1}$, (e) contribution of $-\frac{1}{2}\frac{\partial^2 r_e\left(\overline{R_{0.86}},\overline{R_{2.1}}\right)}{\partial R_{0.86}\partial R_{2.1}}\cdot \text{cov}(R_{0.86},R_{2.1})$ to $\Delta r_{e,2.1}$, (f) contribution of $-\frac{1}{2}\frac{\partial^2 r_e\left(\overline{R_{0.86}},\overline{R_{2.1}}\right)}{\partial R_{2.1}^2}\cdot\sigma_{2.1}^2$ to $\Delta r_{e,2.1}$, (g) contribution of $-\frac{1}{2}\frac{\partial^2 \tau\left(\overline{R_{0.86}},\overline{R_{3.7}}\right)}{\partial R_{3.7}^2}\cdot\sigma_{3.7}^2$ to $\Delta r_{e,3.7}$, (h) contribution of $-\frac{1}{2}\frac{\partial^2 r_e\left(\overline{R_{0.86}},\overline{R_{3.7}}\right)}{\partial R_{0.86}\partial R_{3.7}}\cdot \text{cov}(R_{0.86},R_{3.7})$ to $\Delta r_{e,3.7}$, and (i) contribution of $-\frac{1}{2}\frac{\partial^2 r_e\left(\overline{R_{0.86}},\overline{R_{3.7}}\right)}{\partial R_{3.7}^2}\cdot\sigma_{3.7}^2$ to $\Delta r_{e,2.1}$.

100 m reflectances are shown in Figures 8b and 8c. For the sake of consistency with the notations used in section 3, we refer to these retrievals as subpixel retrievals, i.e., $\tau(R_{0.86,i}, R_{2.1,i})$, $r_e(R_{0.86,i}, R_{2.1,i})$, and $r_e(R_{0.86,i}, R_{3.7,i})$. Results of the τ, $r_{e,2.1}$, and $r_{e,3.7}$ retrievals based on aggregated 400 m reflectances are shown in Figures 8d–8f, respectively, which are referred to as pixel level retrievals $\tau\left(\overline{R_{0.86,i}}, \overline{R_{2.1,i}}\right)$, $r_e\left(\overline{R_{0.86,i}}, \overline{R_{2.1,i}}\right)$, and $r_e\left(\overline{R_{0.86,i}}, \overline{R_{3.7,i}}\right)$.

Having derived both subpixel and pixel level retrievals, we first compute the biases caused by the homogenous pixel assumption, $\Delta\tau$ and Δr_e, as expressed in equation (3). The results are shown in Figures 9a–9c. It can be seen that $\Delta\tau$ is mostly negative over the whole domain, as one would expect based on the PPHB. However, derived values of Δr_e, especially $\Delta r_{e,2.1}$, are predominantly positive, which is the opposite of the PPHB but consistent with the findings in *Zhang and Platnick* [2011] and *Zhang et al.* [2012]. It should be pointed out that the cloud-free pixels are marked in black in the figure. The pixels in gray are partly cloudy pixels (i.e., one or more 100 m subpixels are cloud free), while cloud-free pixels are
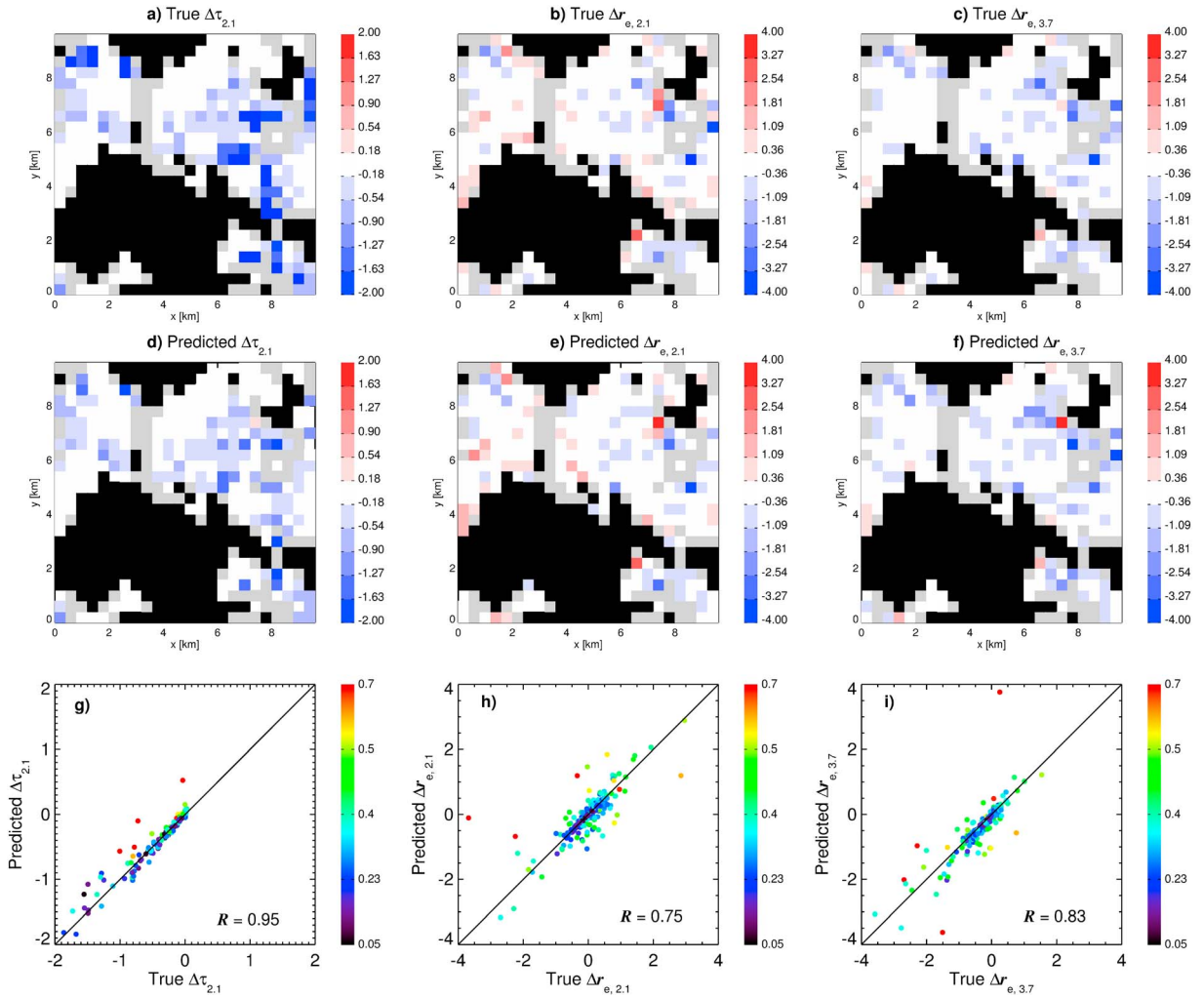
Figure 11. Same as Figure 9 except that in this case the solar zenith angle is 60°.

marked in black. Because it is uncertain how cloud-free subpixels should be treated in the spatial averages, partly cloudy pixels are excluded from our analysis.

To assess the accuracy of our framework, we derived the second set of $\Delta\tau$ and Δr_e based on equation (8) using the matrix of second derivatives (Figures 3 and 4) and the subpixel reflectance variances and covariances (Figure 6). The results from this method are shown in Figures 9d–9f. Evidently, $\Delta\tau$ and Δr_e derived in two different and independent ways agree very well. The correlation coefficients all exceed 0.8 as shown in Figures 9g–9i. Only those pixels with large subpixel inhomogeneity index $H_{\sigma_{0.86}}$ (>0.5) deviate from the one-to-one line. For these pixels the higher-order terms $O(\Delta R^3)$, which were ignored in equation (8), likely impact $\Delta\tau$ and Δr_e. But such cases are relatively rare for this LES scene. The overall excellent agreement clearly demonstrates that our framework is able to provide an accurate quantitative estimation of the biases in τ and r_e retrievals caused by the homogenous pixel assumption for overcast pixels.

One advantage of using equation (8) is that the bias can be further decomposed into the contributions from each term in the matrix of second derivatives, which help us to better understand the relative importance of various factors in causing the bias. For example, as shown in Figures 10a–10c, the τ retrieval bias is dominated by the $-\frac{1}{2}\frac{\partial^2\tau\left(\overline{R_{VIS}},\overline{R_{SWIR}}\right)}{\partial R_{VIS}^2}\cdot\sigma_{VIS}^2$ term in equation (7). As mentioned before, this term corresponds to the PPHB (Figure 2a), which is why the total $\Delta\tau$ in Figure 9 is generally negative. In the case of the $r_{e,3.7}$ retrieval, both the positive $-\frac{1}{2}\frac{\partial^2 r_e\left(\overline{R_{VIS}},\overline{R_{SWIR}}\right)}{\partial R_{VIS}^2}\cdot\sigma_{VIS}^2$ term (Figure 10g) and the negative $-\frac{1}{2}\frac{\partial^2 r_e\left(\overline{R_{VIS}},\overline{R_{SWIR}}\right)}{\partial R_{SWIR}^2}\cdot\sigma_{SWIR}^2$ term
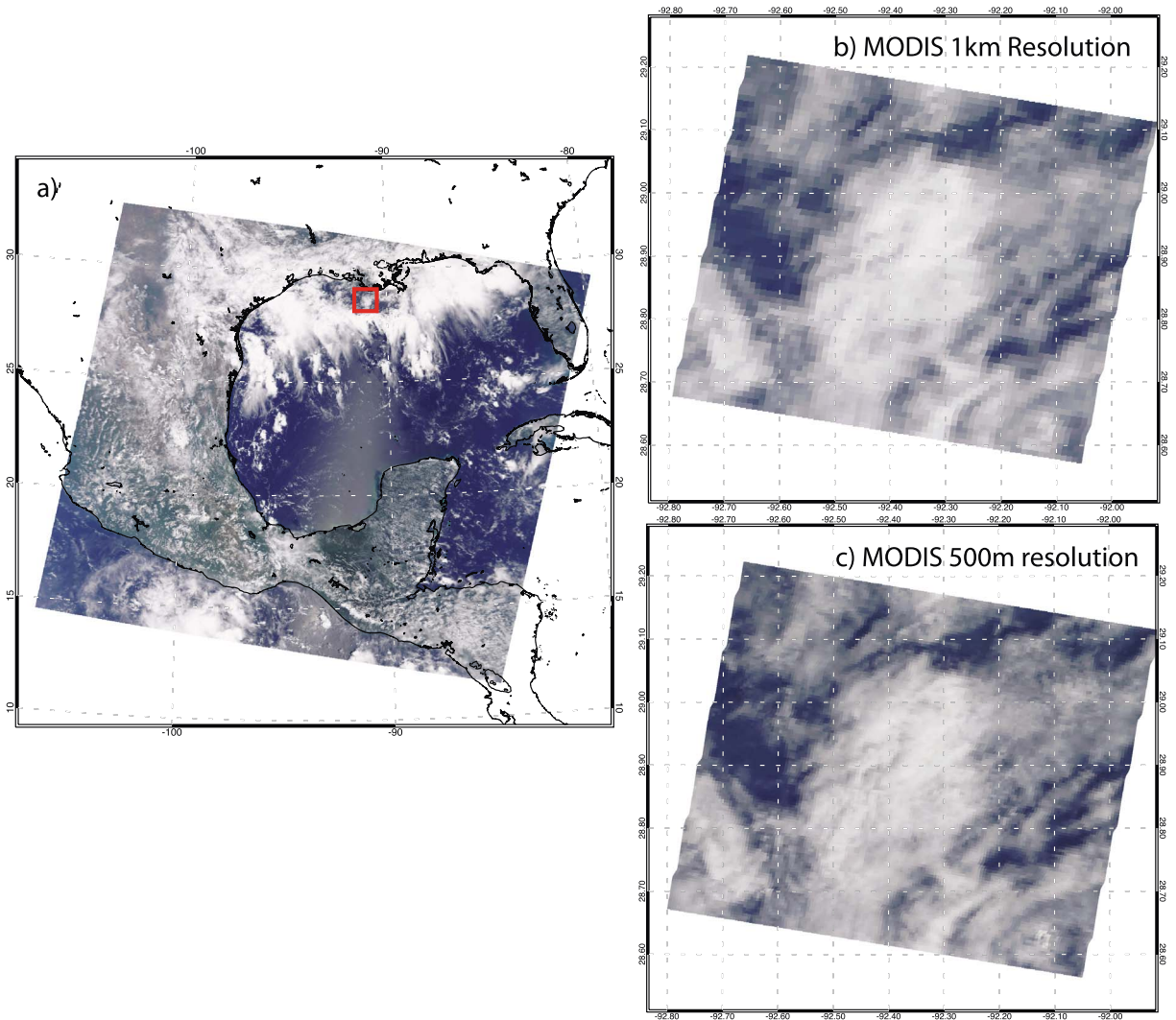
Figure 12. (a) RGB image of a MODIS granule collected over the Gulf of Mexico on 9 September 2006. A zoom-in view of the region in the red box showing the (b) 1 km MODIS true color RGB image and (c) 500 m MODIS true color RGB image.

(Figure 10i) are significant. The former corresponds to the example in Figure 2c, while the latter refers to the example in Figure 2b. After summation, the $-\frac{1}{2}\frac{\partial^2 r_e(\overline{R_{VIS}},\overline{R_{SWIR}})}{\partial R_{VIS}^2}\sigma_{VIS}^2$ term is dominant and leads to the overall positive bias in the $r_{e,3.7}$ retrieval. The bias in the $r_{e,2.1}$ retrieval is even more complicated, as all three terms on the right-hand side of equation (6) contribute substantially to the overall bias. Overall, the positive terms in Figures 10d and 10e dominate the total error budget, leading to a generally positive $\Delta r_{e,2.1}$ in Figure 8.

In the above example, the solar zenith angle is high with $\theta_0 = 20°$. We also tested our framework in a case with low solar zenith angle of $\theta_0 = 60°$, and the results are shown in Figure 11. Evidently, the correlation coefficients between the numerical simulations and those predicted by our framework are very high, suggesting that our framework works equally well in this case.

From the above examples, one can clearly see that our framework provides a comprehensive explanation of the impact of subpixel inhomogeneity on τ and r_e retrievals. As mentioned earlier we have also tested our framework on the retrievals based on reflectances using 1-D radiative transfer and find the predicted $\Delta\tau$ and Δr_e based on our framework to agree very well with the numerical results (not shown).
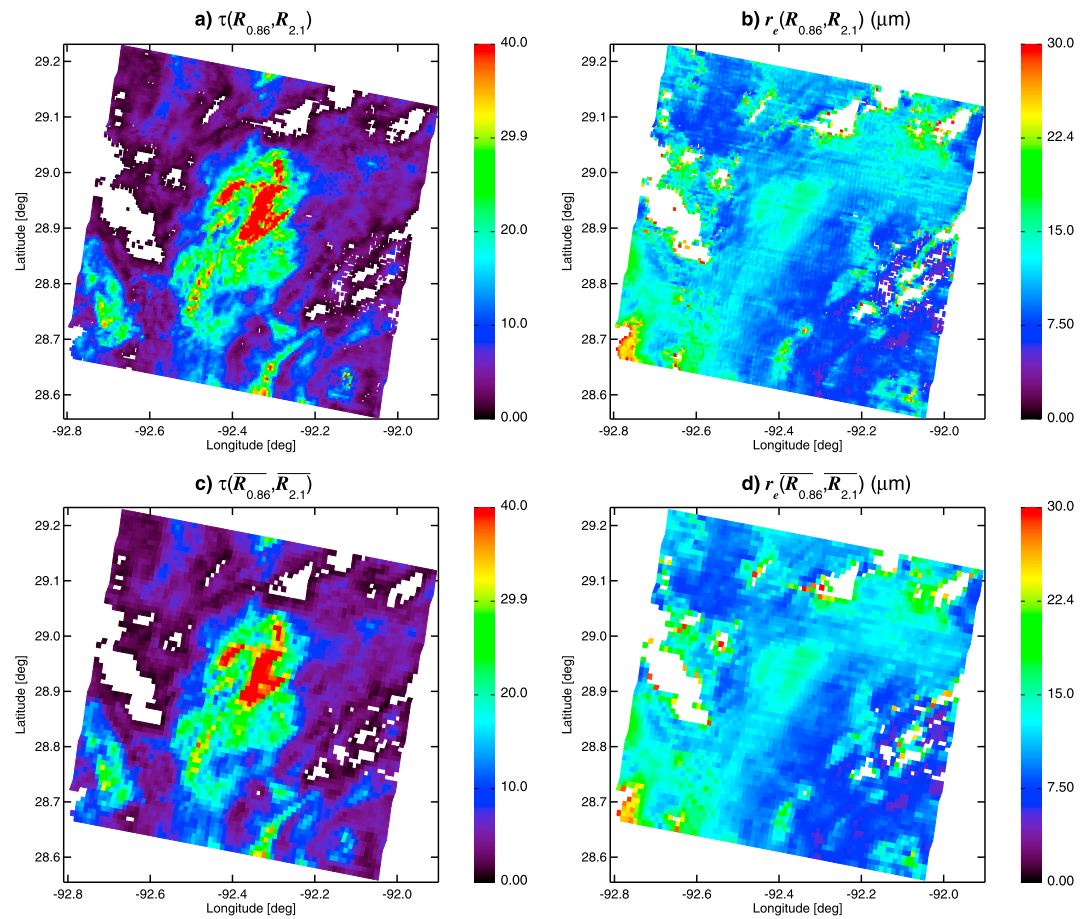
Figure 13. Retrievals of (a) τ and (b) $r_{e,2.1}$ at the 500 m resolution for the region in Figure 12b. Retrieved (c) τ and (d) $r_{e,2.1}$ at the 1 km resolution.

We would like to point out here that less sensitivity to subpixel heterogeneity in the 3.7 μm channel should not necessarily be equated to less r_e bias in the overall retrieval. For simplicity, our 3.7 μm analysis deals with reflectance only. Thus, it assumes that the cloud and surface temperatures are known without error, as are the atmospheric emission/correction terms, needed to infer cloud top reflectance from top-of-atmosphere measurements that contain both emitted and reflected energy. Because we are dealing with reflectance only, an implicit assumption is that the effect of subpixel heterogeneity on the cloud temperature retrieval and atmospheric correction are negligible. The validity of this assumption will be assessed in a future study.

4.2. MODIS Retrieval Test

In the second example, we test our framework using MODIS observations. The MODIS instrument has 36 spectral bands. The spatial resolution of most bands (bands 8–36) is 1 km. Bands 3–7 have a 500 m resolution. Bands 1 and 2 have a 250 m spatial resolution. The current (collection 06) operational MODIS cloud property retrieval products, such as τ, r_e, and LWP, are made at 1 km resolution. The higher spatial resolution of the 0.86 μm (band 2) and 2.1 μm (band 7) sensors provides us with an opportunity to test our framework and investigate the impact of subpixel inhomogeneity on the MODIS τ and r_e retrievals. For this purpose, we selected a case shown in Figure 12. The granule in Figure 12a was collected by MODIS on board the Terra satellite on 9 September 2006 over the Gulf of Mexico. We further selected a small region off the coast of Louisiana marked in the red box for our test. A zoom-in view of this small region at the 1 km and 500 m resolutions is shown in Figures 12b and 12c, respectively.

Similar to the LES example, we first developed two sets of cloud property retrievals, one at a higher spatial resolution of 500 m and the other at a coarser resolution of 1 km. Figures 13a and 13b show the 500 m resolution τ
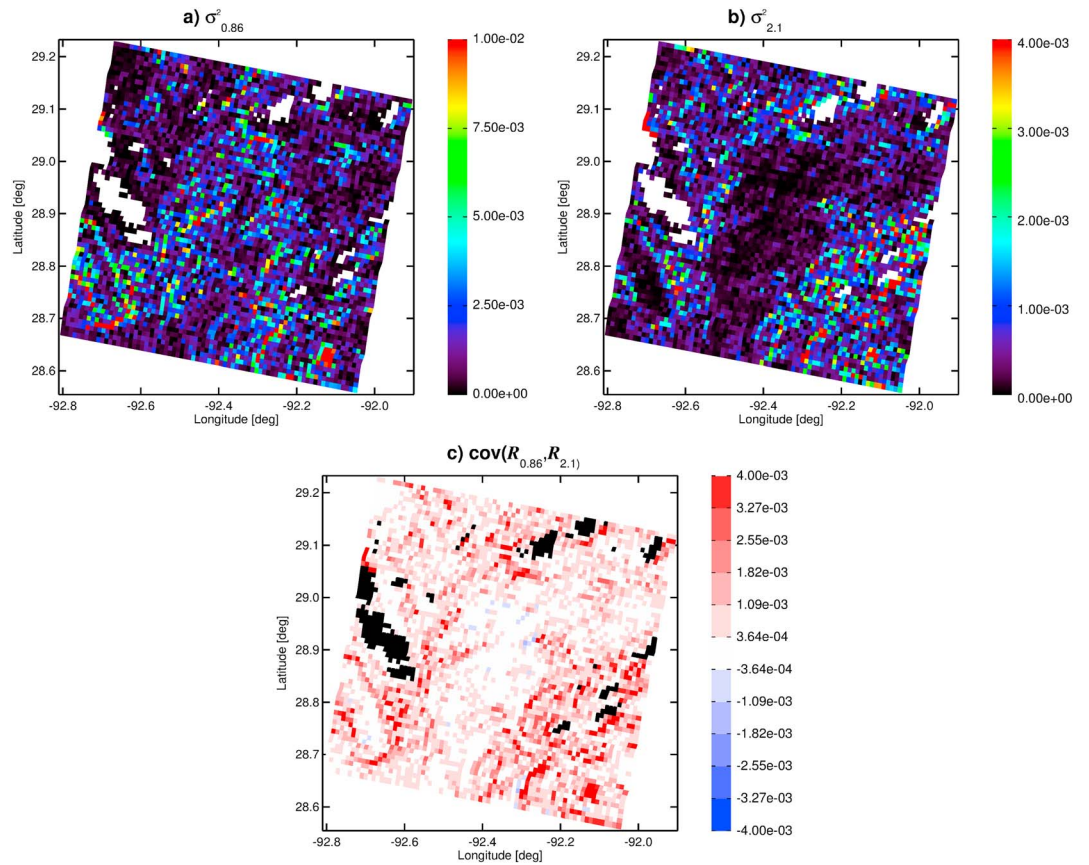
Figure 14. The subpixel reflectance variances (a) $\sigma^2_{0.86}$ and (b) $\sigma^2_{2.1}$ and covariances (c) cov($R_{0.86}, R_{2.1}$) for the MODIS case in Figure 12b.

and r_e retrievals, respectively, based on the combination of 0.86 and 2.1 μm reflectances for the selected region in Figure 12c. The 1 km retrievals are shown in Figures 13c and 13d. This scene has a cloud fraction of about 72%. In the center of the scene is a cluster of thick clouds with τ around 20 to 40 and r_e ranging mainly between 10 μm to 20 μm. Note that in our framework the 500 m retrievals are the subpixel $\tau(R_{VIS,i}, R_{SWIR,i})$ and $r_e(R_{VIS,i}, R_{SWIR,i})$. The 1 km retrievals are $\tau(\overline{R_{VIS}}, \overline{R_{SWIR}})$ and $r_e(\overline{R_{VIS}}, \overline{R_{SWIR}})$. To derive the $\Delta\tau$ and Δr_e from our mathematical framework in equation (8), we compute the subpixel reflectance variances and covariances for every 1 km cloudy pixel from the 2×2 500 m subpixel reflectance observations. The results are shown in Figure 14. Similar to the LES case, we find that the 0.86 and 2.1 μm cloud reflectances are generally positively correlated over the thin cloud regions. The correlation becomes weak (close to zero) over the thick cloud regions. These results indicate that when the cloud is thin, the variability in both 0.86 and 2.1 μm bands is controlled mainly by τ. The variability of 2.1 μm cloud reflectances becomes primarily sensitive to r_e when the cloud becomes optically thick.

The difference between the 1 km retrievals and the mean of 500 m retrievals are the biases, $\Delta\tau$ and Δr_e, caused by the homogeneous pixel assumption. Figures 15a and 15b show $\Delta\tau$ and Δr_e, respectively, based on equation (3). We found that $\Delta\tau$ is mainly negative particularly in the regions with thick clouds, while Δr_e is mainly positive particularly in the transition regions from thick to thin clouds. These results are very similar to what we found in the LES scene in Figure 9. Predicted $\Delta\tau$ and Δr_e, based on equation (8), are shown in Figures 15c and 15d, respectively. The results for both parameters agree reasonably well with the results derived from the numerical retrievals in Figures 15 and 15b. The predicted $\Delta\tau$ based on equation (8) and the numerical results have a correlation coefficient of 0.89 for all cloudy pixels (0.96 for pixels with $\tau > 5$). The correlation coefficient for Δr_e is significantly lower especially for thin clouds with $\tau < 5$. This is mainly because when the cloud is thin, the 2.1 μm cloud reflectances are not very sensitive to r_e. As a result, the retrievals are subject to large uncertainties caused by radiative transfer model uncertainties. If we limited the comparison to clouds with $\tau > 5$ only, the correlation coefficient is 0.72.
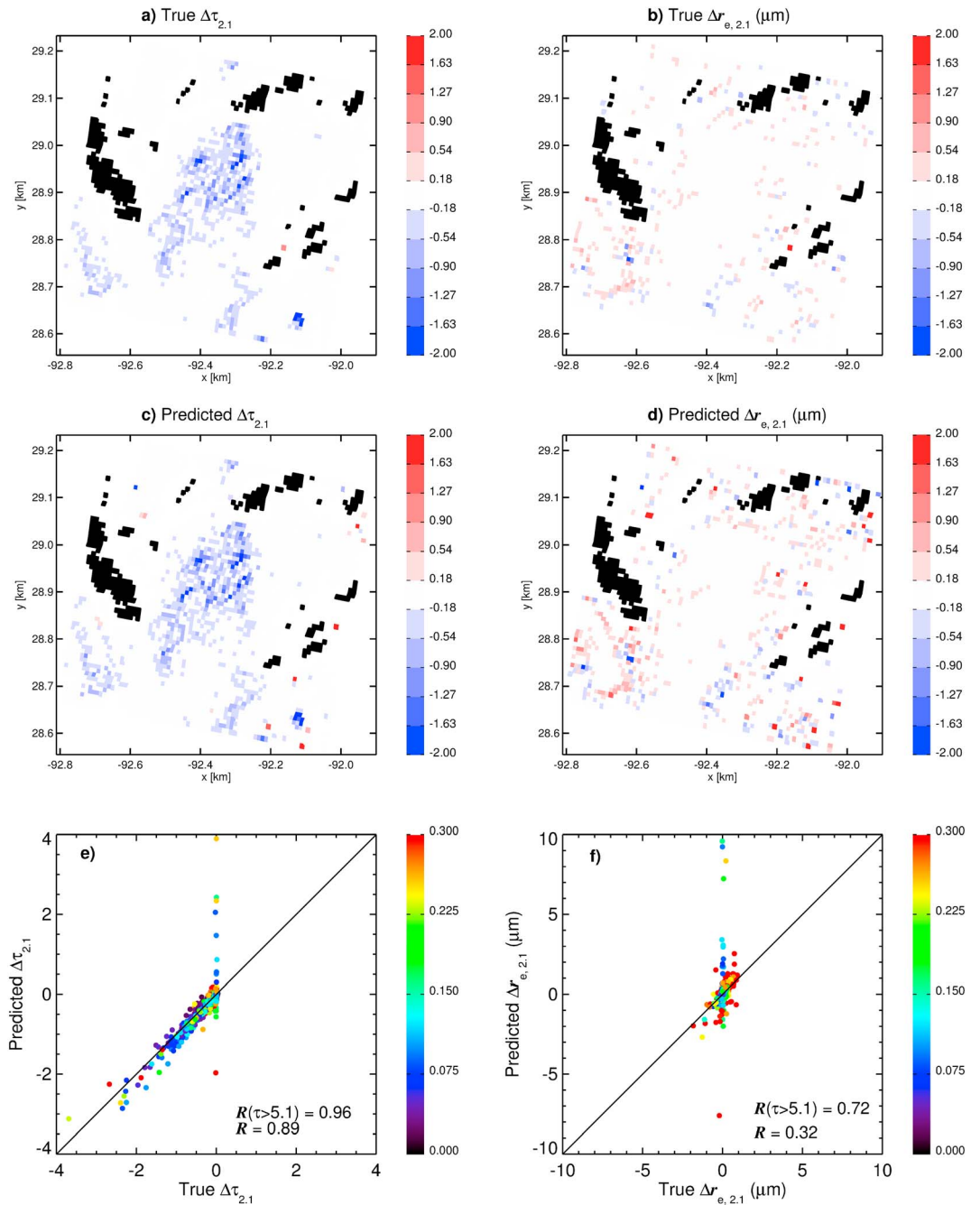
Figure 15. Derived (a) $\Delta\tau$ and (b) Δr_e based on equation (3). (c and d) The corresponding results based on equation (8). (e and f) Pixel-to-pixel comparisons.

In summary, our numerical framework works very well for the LES cases, indicating that the high-order terms are mostly negligible in these cases. It also works reasonably well for the real MODIS case, especially for clouds with $\tau > 5$. For thinner clouds, it is difficult to tell whether the deviation is due to higher-order terms or retrieval uncertainties. Another factor to consider is that we only have four 500 m subpixels for each 1 km pixel, which may not be enough when deriving the subpixel variance and covariance. As part of the ongoing research, we are trying to retrieve τ and r_e from the Advanced Spaceborne Thermal Emission and Reflection Radiometer (ASTER) on bard Terra. ASTER has a much higher resolution than MODIS and therefore can provide much richer information on the small-scale variability of cloud reflectance [*Zhao and Di Girolamo*, 2006; *Wen et al.*, 2007]. We will further test our framework using ASTER observations in future studies.

5. Summary and Discussion

The impact of unresolved subpixel level variation of cloud reflectances is an important source of uncertainty in the bispectral solar reflective method. In this study, we develop a mathematical framework for understanding this impact and quantifying the consequent biases, $\Delta\tau$ and Δr_e. We show in equation (8) that $\Delta\tau$ and Δr_e are determined by two factors: the nonlinearity of the LUT and the inhomogeneity of reflectances within the pixel. We test our framework using LES cloud fields and real MODIS observations. The results indicate that in comparison with previous studies, our framework provides a more comprehensive explanation and more accurate estimation of the retrieval biases caused by the subpixel level variation of cloud reflectances. Most importantly, it demonstrates that subpixel variations in cloud reflectance can lead to both positive and negative values of Δr_e. In both the LES and MODIS case that we examined, Δr_e are dominantly positive, hence contributing to the dominantly positive bias in retrieved r_e from resolved cloud variability.

Our framework could have several applications. For example, it can be used to understand the differences between retrievals made at different spatial resolutions (e.g., MODIS versus SEVIRI) or based on different spectral reflectances (e.g., MODIS 2.1 μm versus 3.7 μm). It could also be useful for estimating retrieval uncertainties. For example, the retrieval uncertainty caused by subpixel reflectance variations in the operational 1 km MODIS cloud products can be estimated from the 500 m cloud reflectances based on our framework. It can also be integrated into the operational MODIS retrieval algorithm to determine in real time whether the high-resolution retrievals (e.g., from 1 km to 500 m) are necessary for a given pixel. Another useful application is to help the trade-off studies for instrument design. For example, the Ocean Color Imager (OCI) is the key instrument planned for NASA's coming Pre-Aerosol, Clouds, and ocean Ecosystem mission (http://decadal.gsfc.nasa.gov/pace.html). An important part of the OCI deign trade-off study is to determine the optimal space resolution for both ocean color and atmospheric observations, including cloud property retrievals. Our framework would be highly useful for such a study.

Finally, we feel it is necessary to clarify again that our framework cannot explain or predict 3-D radiative effects, such as the illuminating effect, shadowing effect, and photon leaking effect, which are known to have a substantial influence on cloud reflectances and therefore retrieval results. These effects are beyond the scope of this study. Our framework simply predicts the statistical differences between the retrievals with difference spatial resolutions, regardless whether the radiative transfer is 1-D or 3-D.

References

Ackerman, A. S., M. P. Kirkpatrick, D. E. Stevens, and O. B. Toon (2004), The impact of humidity above stratiform clouds on indirect aerosol climate forcing, *Nature*, *432*(7020), 1014–1017, doi:10.1038/nature03174.

Barker, H. W. (1996), A parameterization for computing grid-averaged solar fluxes for inhomogeneous marine boundary layer clouds. Part I: Methodology and homogeneous biases, *J. Atmos. Sci.*, *53*(16), 2289–2303, doi:10.1175/1520-0469(1996)053<2289:APFCGA>2.0.CO;2.

Cahalan, R. F., and J. H. Joseph (1989), Fractal statistics of cloud fields, *Mon. Weather Rev.*, *117*(2), 261–272.

Cahalan, R. F., W. Ridgway, W. J. Wiscombe, T. L. Bell, and J. B. Snider (1994), The albedo of fractal stratocumulus clouds, *J. Atmos. Sci.*, *51*(16), 2434–2455, doi:10.1175/1520-0469(1994)051<2434:TAOFSC>2.0.CO;2.

Cho, H. M., et al. (2015), Frequency and causes of failed MODIS cloud property retrievals for liquid phase clouds over global oceans, *J. Geophys. Res. Atmos.*, *120*, 4132–4154, doi:10.1002/2015JD023161.

Davis, A., and A. Marshak (2010), 3D transport of solar radiation in clouds, *Rep. Prog. Phys.*

Di Girolamo, L., L. Liang, and S. Platnick (2010), A global view of one-dimensional solar radiative transfer through oceanic water clouds, *Geophys. Res. Lett.*, *37*, L18809, doi:10.1029/2010GL044094.

Dong, X., T. P. Ackerman, E. E. Clothiaux, P. Pilewskie, and Y. Han (1997), Microphysical and radiative properties of boundary layer stratiform clouds deduced from ground-based measurements, *J. Geophys. Res.*, *102*(D20), 23,829–23,843, doi:10.1029/97JD02119.

Harshvardhan, and D. A. Randall (1985), Comments on "The parameterization of radiation for numerical weather prediction and climate models", *Mon. Weather Rev.*, *113*(10), 1832–1833, doi:10.1175/1520-0493(1985)113<1832:COPORF>2.0.CO;2.

Kato, S., L. M. Hinkelman, and A. Cheng (2006), Estimate of satellite-derived cloud optical thickness and effective radius errors and their effect on computed domain-averaged irradiances, *J. Geophys. Res.*, *111*, D17201, doi:10.1029/2005JD006668.

Liang, L., and L. D. Girolamo (2013), A global analysis on the view-angle dependence of plane-parallel oceanic liquid water cloud optical thickness using data synergy from MISR and MODIS, *J. Geophys. Res. Atmos.*, *118*, 2389–2403, doi:10.1029/2012JD018201.

Liang, L., L. Di Girolamo, and S. Platnick (2009), View-angle consistency in reflectance, optical thickness and spherical albedo of marine water-clouds over the northeastern Pacific through MISR-MODIS fusion, *Geophys. Res. Lett.*, *36*, L09811, doi:10.1029/2008GL037124.

Liang, L., L. Di Girolamo, and W. Sun (2015), Bias in MODIS cloud drop effective radius for oceanic water clouds as deduced from optical thickness variability across scattering angles, *J. Geophys. Res. Atmos.*, *120*, 7661–7681, doi:10.1002/2015JD023256.

Marshak, A., S. Platnick, T. Várnai, G. Wen, and R. F. Cahalan (2006), Impact of three-dimensional radiative effects on satellite retrievals of cloud droplet sizes, *J. Geophys. Res.*, *111*, D09207, doi:10.1029/2005JD006686.

Minnis, P., et al. (2011), CERES edition-2 cloud property retrievals using TRMM VIRS and Terra and Aqua MODIS data—Part I: Algorithms, *IEEE Trans. Geosci. Remote Sens.*, *49*(11), 4374–4400, doi:10.1109/TGRS.2011.2144601.

Nakajima, T., and M. D. King (1990), Determination of the optical thickness and effective particle radius of clouds from reflected solar radiation measurements. Part I: Theory, *J. Atmos. Sci.*, *47*(15), 1878–1893, doi:10.1175/1520-0469(1990)047<1878:DOTOTA>2.0.CO;2.

Oreopoulos, L., and R. Davies (1998), Plane parallel albedo biases from satellite observations. Part I: Dependence on resolution and other factors, *J. Clim.*, *11*(5), 919–932.

Oreopoulos, L., R. F. Cahalan, and S. Platnick (2007), The plane-parallel albedo bias of liquid clouds from MODIS observations, *J. Clim.*, *20*(20), 5114–5125, doi:10.1175/JCLI4305.1.

Painemal, D., and P. Zuidema (2011), Assessment of MODIS cloud effective radius and optical thickness retrievals over the Southeast Pacific with VOCALS-REx in situ measurements, *J. Geophys. Res.*, *116*, D24206, doi:10.1029/2011JD016155.

Pincus, R., and K. F. Evans (2009), Computational cost and accuracy in calculating three-dimensional radiative transfer: Results for new implementations of Monte Carlo and SHDOM, *J. Atmos. Sci.*, *66*(10), 3131–3146, doi:10.1175/2009JAS3137.1.

Pincus, R., S. A. McFarlane, and S. A. Klein (1999), Albedo bias and the horizontal variability of clouds in subtropical marine boundary layers: Observations from ships and satellites, *J. Geophys. Res.*, *104*(D6), 6183–6191, doi:10.1029/1998JD200125.

Platnick, S., M. D. King, S. A. Ackerman, W. P. Menzel, B. A. Baum, J. C. Riédi, and R. A. Frey (2003), The MODIS cloud products: Algorithms and examples from Terra, *IEEE Trans. Geosci. Remote Sens.*, *41*(2), 459–473, doi:10.1109/TGRS.2002.808301.

Roebeling, R., A. Feijt, and P. Stammes (2006), Cloud property retrievals for climate monitoring: Implications of differences between Spinning Enhanced Visible and Infrared Imager (SEVIRI) on METEOSAT-8 and Advanced Very High Resolution Radiometer (AVHRR) on NOAA-17, *J. Geophys. Res.*, *111*, D20210, doi:10.1029/2005JD006990.

Stamnes, K., S. Tsay, K. Jayaweera, and W. Wiscombe (1988), Numerically stable algorithm for discrete-ordinate-method radiative transfer in multiple scattering and emitting layered media, *Appl. Opt.*, *27*(12), 2502–2509.

Stevens, D. E., A. S. Ackerman, and C. S. Bretherton (2010), Effects of domain size and numerical resolution on the simulation of shallow cumulus convection, *J. Atmos. Sci.*, *59*(23), 3285–3301, doi:10.1175/1520-0469(2002)059<3285:EODSAN>2.0.CO;2.

Várnai, T., and A. Marshak (2002), Observations of three-dimensional radiative effects that influence MODIS cloud optical thickness retrievals, *J. Atmos. Sci.*, *59*(9), 1607–1618, doi:10.1175/1520-0469(2002)059<1607:OOTDRE>2.0.CO;2.

Walther, A., and A. K. Heidinger (2012), Implementation of the Daytime Cloud Optical and Microphysical Properties Algorithm (DCOMP) in PATMOS-x, *J. Appl. Meteorol. Climatol.*, *51*(7), 1371–1390, doi:10.1175/JAMC-D-11-0108.1.

Wen, G., A. Marshak, R. F. Cahalan, L. A. Remer, and R. G. Kleidman (2007), 3-D aerosol-cloud radiative interaction observed in collocated MODIS and ASTER images of cumulus cloud fields, *J. Geophys. Res.*, *112*, D13204, doi:10.1029/2006JD008267.

Zhang, Z. (2013), On the sensitivity of cloud effective radius retrieval based on spectral method to bi-modal droplet size distribution: A semi-analytical model, *J. Quant. Spectros. Radiat. Transfer*, *129*, 79–88, doi:10.1016/j.jqsrt.2013.05.033.

Zhang, Z., and S. Platnick (2011), An assessment of differences between cloud effective particle radius retrievals for marine water clouds from three MODIS spectral bands, *J. Geophys. Res.*, *116*, D20215, doi:10.1029/2011JD016216.

Zhang, Z., A. S. Ackerman, G. Feingold, S. Platnick, R. Pincus, and H. Xue (2012), Effects of cloud horizontal inhomogeneity and drizzle on remote sensing of cloud droplet effective radius: Case studies based on large-eddy simulations, *J. Geophys. Res.*, *117*, D19208, doi:10.1029/2012JD017655.

Zhao, G., and L. Di Girolamo (2006), Cloud fraction errors for trade wind cumuli from EOS-Terra instruments, *Geophys. Res. Lett.*, *33*, L20802, doi:10.1029/2006GL027088.